UNIVERSITÀ
DEGLI STUDI
FIRENZE

School of
Mathematical
Physical and Natural
Sciences

Master Degree in
Advanced Molecular Sciences

Structural characterization of bioinspired inorganic oxides

Caratterizzazione strutturale di ossidi inorganici bioispirati

Supervisor
Enrico Ravera

Co-Supervisor
Ilaria Palchetti

Candidate
Francesco Bruno

Academic Year 2020/2021

Contents

List of Figures

A Letizia

1. Introduction

Chemical reactions are defined as processes that lead to the interconversion of chemical species, driven by the lowering of free energy when the reactants are transformed into the products. Under these conditions, the reaction is said to be thermodynamically favoured, and therefore spontaneous. However, in the majority of cases several steps are required to achieve the final result, i.e. the reactants undergo transformations through a number of higher energy transition states and intermediates during the process. In order to understand if the occurring of a chemical reaction is actually possible, it is necessary to describe its kinetics.

The rate constant k of a single-step chemical reaction (or of a multi-step chemical reaction in the rate limiting step approximation) is rationalized through the Arrhenius equation, according to which the reaction rate constant shows an exponential behaviour with respect to the ratio between activation energy of the reaction ΔE_a and thermal energy $k_B T$ (equation 1.1, figure 1.1).

$$k = A\, e^{-\Delta E_a / k_B T} \tag{1.1}$$

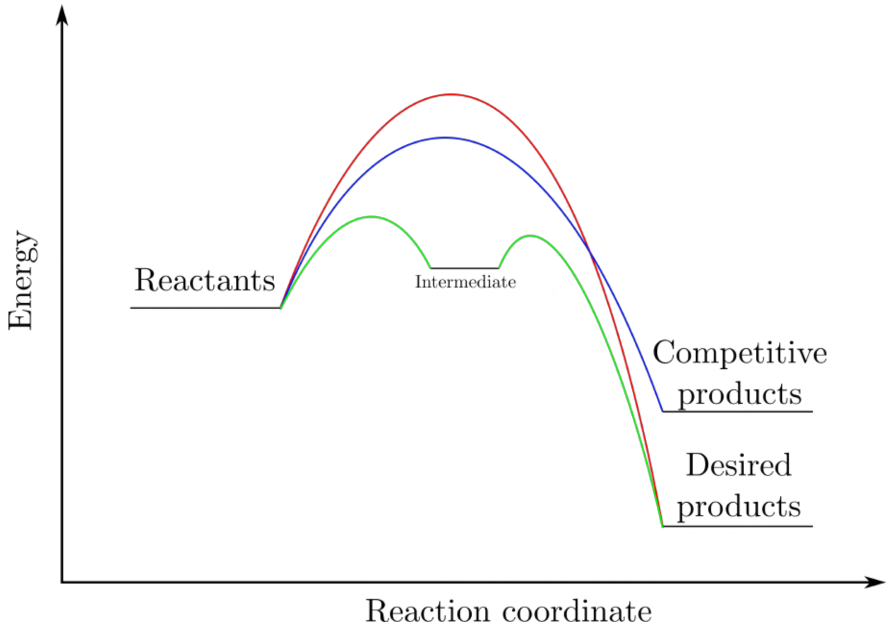

Figure 1.1: Scheme illustrating various pathways that a chemical reaction may undergo. Red – desired pathway without catalyst, blue – kinetically competing pathway, green – pathway with catalyst.

It is not uncommon that the products of a chemical reaction are not observed by the simple mixing of the reactants because of the too high activation energy.

Given that increasing the temperature is often not an economically viable option, and the number of competing reactions can increase significantly, the activation energy is reduced introducing inside the reaction vessel a catalytic compound. The employment of the right catalyst improves dramatically the yields of a chemical reactions by either deviating its pathway, providing an alternative transition state with a lower activation energy, or enhancing the selectivity towards the reactants.

Nowadays, with the pressing need to improve the sustainability and reducing the environmental footprint of chemical processing, highly efficient catalysts that work under near-ambient conditions and in environmental-friendly solvents are likely to determine the future of chemical industry. One way to make this transition possible is to develop catalysts that are based on immobilized enzymes. Enzymes work in aqueous environment (no use of noxious solvents) under conditions of pressure and temperature that are compatible with life, are efficient and highly selective (atom-economy) and, through immobilization, they become easily separable and highly stable (reduce and reuse).

It has been proposed that the best route for the preparation of such hybrid catalysts is a biomimetic synthesis, through which the assembly of the support and the encapsulation of the active enzyme are achieved in a single reaction step[1]. In fact, the preparation of bioinspired inorganic oxides has attracted noticeable interest since it allows the generation of a wide plethora of composite materials, whose structure and reactivity is tunable, keeping the production costs incredibly low without the employment of the harsh conditions required for classical production of such compounds. When proteins are bound to or entrapped inside a material usually result stabilized and, in turn, the material gains peculiar reactivity properties[2,3].

As the hybrid interfaces between inorganic support and protein are non-crystalline in nature, the methods usually employed for the characterization of solids like X-ray diffraction cannot be used. Another limitation is that the matrix is usually more electron-dense than the protein, limiting the applicability of Cryo-EM. Therefore, solid state Nuclear Magnetic Resonance (ssNMR) represents the ideal technique to interrogate the short and medium-range atomic-level structure, in order to provide a complete description of the obtained composite structure.

The aim of the project is to synthesize a heterogeneous catalyst for the oxidation of organic pollutants, based on cytochrome-c (cyt-c) and titania TiO_2, and to understand deeply its structure and operation mechanism.

1.1 Cytochrome-c

Cytochrome-c (cyt-c) is a small protein whose primary structure is composed of 100 aminoacids (molecular weight: 12 kDa). Its structure is depicted in figure 1.2.

It binds a heme group that coordinates an iron atom, which can be found in various oxidation states[4]. For this reason, cyt-c is involved in the electron transport chain in mitochondria, and it has been demonstrate it is able to catalyze several redox reactions, such for instance hydroxylation, aromatic oxidation, and disposal of peroxides and superoxides.

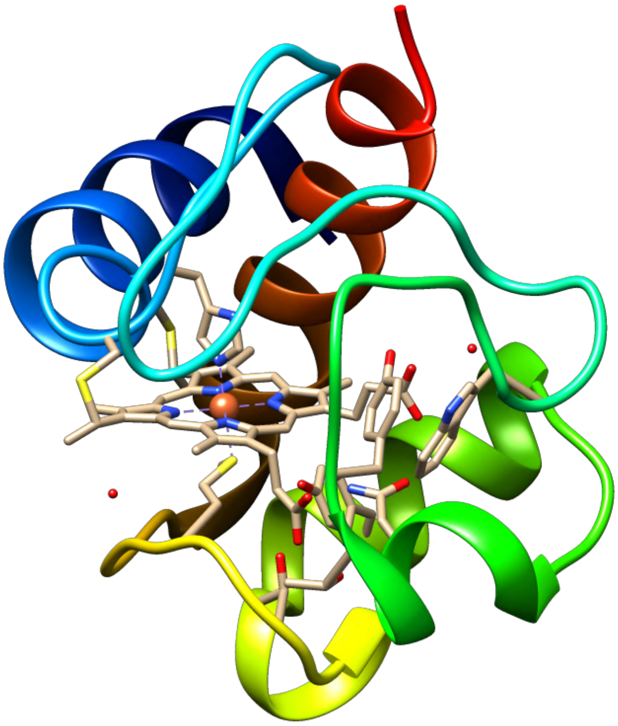

Figure 1.2: Structure of horse heart cytochrome-c, obtained by X-ray diffraction. PDB: 6K9I.

1.2 Titania

Titanium dioxide, TiO_2, is a white solid used as a pigment since ancient times. It is inexpensive, chemically stable, environmentally friendly and bio-compatible, has been widely used in paints, cosmetics, health care products and many other fields of applications. It can be found in nature mainly as three polymorphs: rutile, anatase and brookite. TiO_2 possesses photocatalytic activity upon UV light irradiation[5].

Mesoporous TiO_2 has also been used as support material for the development of high performance heterogeneous catalysts(figure 1.3). In fact, this kind of structure is prone to adsorption and immobilization of small molecules: in this way, the molecules are made more available for exploiting their catalytic activity with respect to the situation in which they are free in solution, because in the latter case the formation of aggregates would cause the sealing of the catalyst active site. Furthermore, anchoring the active molecule to a scaffold improves in general the stability of the final catalyst[6,7].

There are mainly two pathways to synthesize mesoporous titania: the soft-templating method and the hard-templating nanocasting approach.

The soft templating method consists in a co-assembly process of precursors and surfactant templates. The main issue in this approach is that it is not easy to control the reactivity of transition metal precursors, because they are highly sensitive to water and moisture, and tend to fast hydrolyze prior to assembly with the surfactant templates. The first example of mesoporous TiO_2 obtained by this method was reported in 1995 (Ti-TMS1)[8], and in the following years the synthetic approach was refined in order to generate a wide plethora of TiO_2 with different physico-chemical properties. Modified sol-gel method[9], sonochemical method[10] and evaporation-induced self-assembly (EISA)[11] are worth-mention examples.

The suitable Ti sources for the synthesis of mesoporous TiO_2 by soft-templating method are quite limited. Only anhydrous $TiCl_4$, $TiOSO_4$, peroxotitanates and titanium alcoxides have been used. The last one mentioned could be used in aqueous synthesis, but it is still difficult and often a ligand-assisted method is required. Further examples are summarized in table 1.1.

Ti precursor	Template	Meso-structure	T (°C)	Surface area (m^2g^{-1})	Pore size (nm)	Method	Ref.
TIPO	Tetradecyl phosphate	p6mmm	350	200	3.2	Aqueous solution	[8]
Peroxy-titanates	CTAC	p6mm or lamellar	300	310	3.6	Aqueous solution	[9]
TIPO	Octadecyl amine	wormhole-like	350	467	1.5	Aqueous solution, sonochemical	[10]
$TiCl_4$	P123	p6mm	400	205	6.5	EISA	[13]
$TiCl_4$ and TIPO	F108	$Im\bar{3}m$	350	205	6.3	EISA	[14]

Table 1.1: Structural and texture characters of mesoporous TiO_2 synthesized under different conditions. Adapted from reference[12].

The hard-templating approach is usually to prepare mesoporous materials in a confined space, in which the growth of the precursor is restricted to the surface, cages, channels or substrate of a "hard template", such as nanoparticles, colloidal crystals and mesoporous materials.

Successful synthesis of ordered TiO_2 structure has been shown employing SBA-15 silica and titanium nitrate[15] or KIT-6 and titanium alcoxide[16] as hard-templates and precursors, respectively.

In addition to soft- and hard-templating methods, which aim to generate ordered mesoporous TiO_2 structures, there are several synthetic routes for the preparation of disordered mesoporous titania[17,18]. Also biotechnological pathways are viable options.

TiO_2 is photocatalytic because it is able to absorb energy from light. This peculiar reactivity can be directed to (e.g.) catalyze the degradation of organic molecules and of some inorganic pollutants like nitrogen oxides (NO_x). Furthermore, TiO_2 photocatalytic activity has been exploited in several other applications, such as photoelectrolysis of water, wastewater treatment and in medical field. As the photocatalytic activity takes place only on the exposed surface area of TiO_2, the amount of required material can be reduced by depositing a thin layer of titania on a solid substrate.

The process of photocatalysis in titania starts when a photon is absorbed by an electron in the valence band of titania (figure 1.4a)[20,21]. This electron is then excited to the conduction band, leaving a “hole” behind in the valence band (reaction 1.2, figure 1.4b). The valence and conduction bands of titania have the appropriate energy difference for driving many important redox reactions: after the excitation of electrons, holes in the valence band have a redox potential of

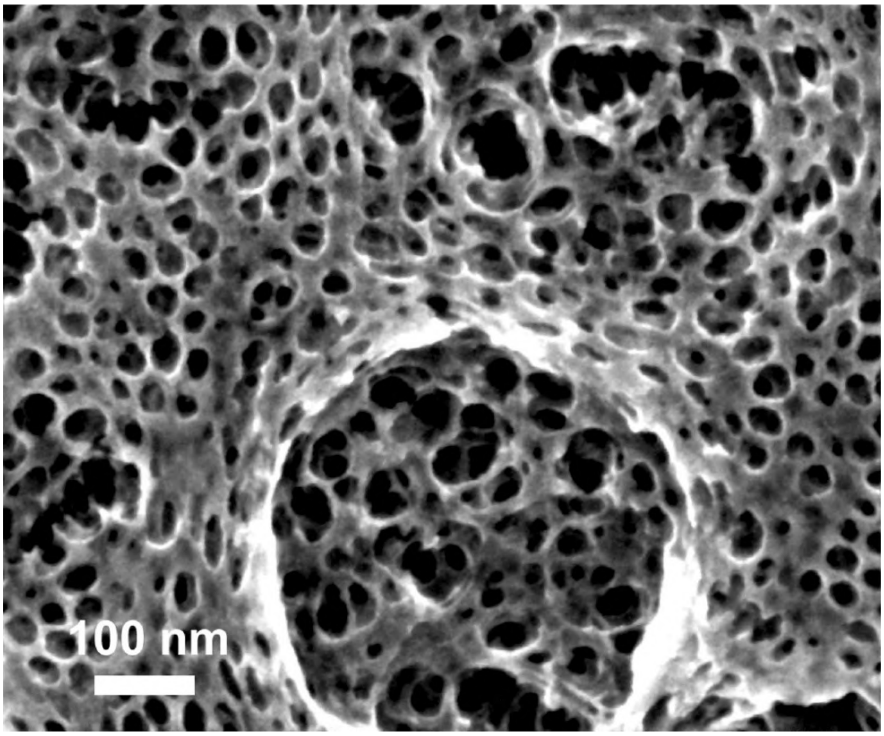

Figure 1.3: SEM image of a TiO_2 thin film, brought as example of porous TiO_2 structure. The macropores are further structured by mesopores, that extend into the bulk of the film[19].

2.53 V, which is enough for the oxidation of hydroxyl ions into hydroxyl radical (reaction 1.3) or the oxidation of adsorbed organic molecules groups, whereas the redox potential of electrons in the conduction band is −0.52 V, which is strong enough to reduce oxygen to superoxide (reaction 1.4, figure 1.4c).

$$\mathrm{TiO_2 + light \longrightarrow TiO_2 + e^- + h^+} \tag{1.2}$$

$$\mathrm{OH^- + h^+ \longrightarrow OH^\bullet} \tag{1.3}$$

$$\mathrm{O_2 + e^- \longrightarrow O_2^-} \tag{1.4}$$

$$\mathrm{O_2 + 2\,H_2O + 2\,e^- \longrightarrow 2\,H_2O_2} \tag{1.5}$$

$$\mathrm{H_2O_2 + e^- \longrightarrow OH^- + OH^\bullet} \tag{1.6}$$

By reacting Ti^{4+} and O^{2-} into Ti^{3+} and O^-, excited electrons and holes can remain at the surface longer if there are no adsorbed species with which they can react directly. Because the difference in charge between titanium and oxygen atoms is then reduced, the oxygen atoms are much less stable and can, with relatively little energy, leave the crystal forming oxygen vacancies. These electron-rich spots make titania a n-type semiconductor, which exhibits higher conductivity with respect to normal titania intrinsic semiconductor. Furthermore, oxygen vacancies make the titania surface more hydrophilic when they are occupied by water molecules, leading to an increase in photocatalytic efficiency[23]. While it is possible that the degradation of organic materials on the surface can also play a role on the hydrophilicity increase, it nevertheless has been shown not to be a determining factor[21].

As mentioned above, titania has several forms, but the two main crystal structures that most researchers focus on are rutile and anatase[20], which are both

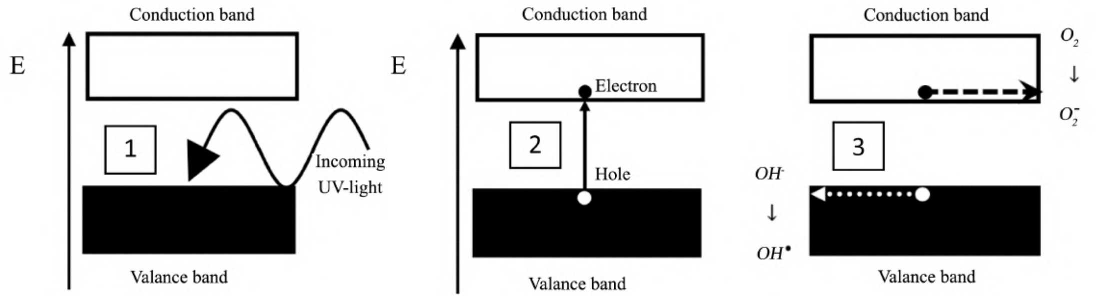

(a) **(b)** **(c)**

Figure 1.4: Schematic drawing of the photocatalytic activity of titania. (a) The absorption of a photon; (b) The excitation of an electron to the conduction band; (c) The transport of the electron and hole from the initial point to reach the surface of titania where the electron and hole can react with an adsorbed molecule. Adapted from reference[22].

tetragonal structures where titanium atoms are hexacoordinated in an octahedral formation. The band gap of rutile and anatase are 3.0 eV and 3.2 eV, respectively. Rutile is able to absorb more light in the visible range than anatase, in fact photocatalysis requires electromagnetic radiation with wavelength shorter than 413 nm for the first and 387 nm for the latter. However, anatase is more photocatalitically active, because excited electrons and holes in anatase can travel farther than in rutile, so that more of them can reach the TiO_2 surface. As proof of this, the maximum film thickness where the photocatalytic efficiency increases with increasing size is 2.5 nm for rutile and 5 nm for anatase.

On the other hand, amorphous titania has the lowest efficiency[24]. The main reason is that in this form there are many spots where recombination of the electron-hole pair can happen. The recombination through defects is in fact the most common way through which electrons and holes are lost. In addition, conductivity in amorphous materials is very low since the energy levels are much more localized. These two effects mean that only electrons excited directly at the surface play a role in the photocatalytic activity of amorphous TiO_2.

For the investigation of TiO_2 structure, the usage of ssNMR is quite complicated due to the spectroscopic properties of magnetically active Ti nuclei: both ^{47}Ti and ^{49}Ti have low gyromagnetic ratios ($\gamma = -2.40\,\mathrm{MHz\,T^{-1}}$), low natural abundance (7.28% for ^{47}Ti and 5.51% for ^{49}Ti) and large quadrupolar coupling constants ($I = 5/2$ and $Q(^{47}\mathrm{Ti}) = 3.2 \cdot 10^{-29}\,\mathrm{m^2}$ and $Q(^{49}\mathrm{Ti}) = 2.5 \cdot 10^{-29}\,\mathrm{m^2}$)[25]. Given that bioinspired reactions (see above) can be used to template the formation of silicon dioxide (SiO_2), we have decided to study the atomic-level morphological properties on scaffolds made of SiO_2 instead of TiO_2 for the composite catalyst, since the magnetically active Si nucleus does not suffer all the problems that affect Ti-NMR.

1.3 Silica

Silicon dioxide SiO_2, also known as silica in traditional nomenclature, is a polymeric solid whose physico-chemical properties resemble those ones of TiO_2. Silica is the main constituent of silicate minerals, but exists also as synthetic product: notable examples include fused quartz, fumed silica and silica gel. It is a chemically inert material, very hard, and unable to conduct heat or electric current. These properties make it ideal for applications in structural materials, microelectronics, analytical chromatography, but also in food and pharmaceutical industry.

SiO_2 can be found in the form of a white crystalline powder, where each silicon atom is coordinated to three oxygen atoms, or in its hydrated form, in which each Si atom coordinates four oxygen atoms in a tetrahedron-like base structure (figure 1.5). In this situation, silicon sites with different hydration degree can be identified: trisilanols $SiO(OH)_3$ (Q^1), disilanols $SiO_2(OH)_2$ (Q^2), monosilanols $SiO_3(OH)$ (Q^3) and fully condensed sites SiO_4 (Q^4).

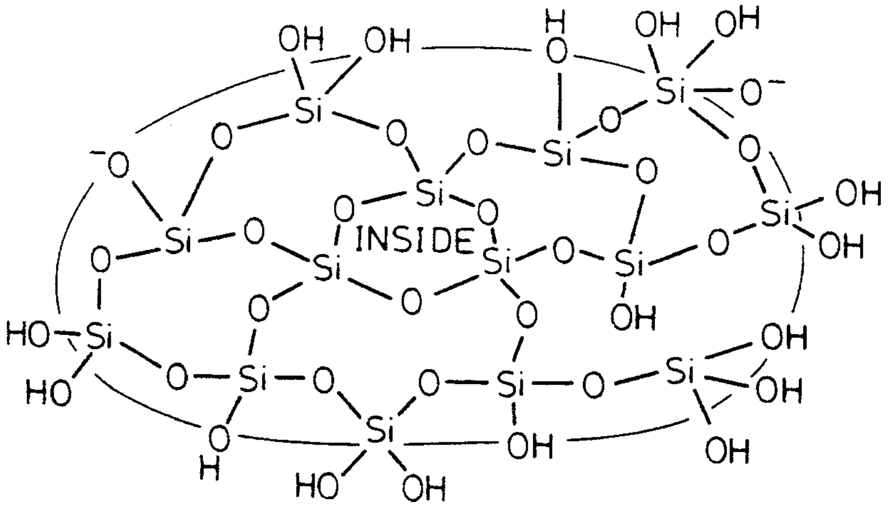

Figure 1.5: Schematic illustration of the nature of amorphous hydrated silica. Notice the different number of OH groups on different silicon atoms, the absence of structural repeat and the few surface charges[26].

Its porous structure makes it particularly suitable for the adsorption of small molecules, just like TiO_2. For this reason, the scaffolding role in composite materials of SiO_2 and TiO_2 is interchangeable.

Bottom-up silica preparation in vitro by tradition exploits the Stöber process, that foresees mixing a silica precursor (normally, an alkyl-silicate) with ammonia in a water/alcohol solution[27]. The alkyl silicate is hydrolyzed to give silicic acid, which subsequently condenses to yield monodispersed nonporous silica particles, that range in size from 50 nm to 2 µm in diameter. A key aspect of the Stöber process resides in the possibility to vary the size of the produced silica particles by altering the reaction conditions, in particular the concentration of the various reactants and their relative amounts.

Modified Stöber processes were developed incorporating surfactants into the synthesis, in order to create porous particles so that to broaden the utility of the produced silica by opening new applications. The electrostatic interactions bring the silica oligomers into greater proximity with each other and, as a result, the silica network condenses around the surfactant micelles, preventing at the same time the aggregation of the forming particles. These electrostatic interactions are pH dependent: some examples are shown in figure 1.6. Surfactants control the morphology, size and porosity of the particles, enabling a high degree of tunability of these physical properties[28].

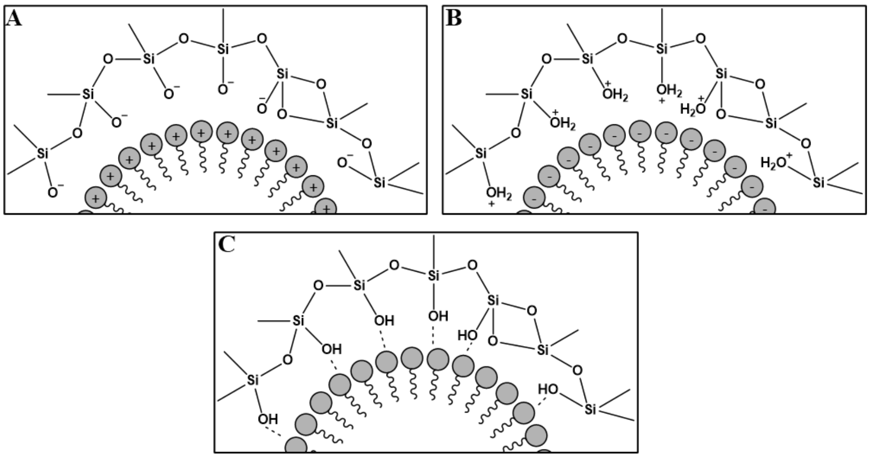

Figure 1.6: Example of (A) interaction of cationic surfactant with negatively charged silicate species in basic conditions, (B) interaction of anionic surfactant with positively charged silicate species in acidic conditions and (C) interaction of non-ionic surfactant with silica through hydrogen bonding. Note: other types of interactions exist, shown here are the three most common[29].

However, this production process is problematic, since many reactants and by-products of Stöber and modified Stöber processes are dangerous when released into the environment. In particular, petrolchemically-derived surfactants like for instance cetyl-trimethylammonium bromide (CTAB) and hexadecylamine (HDA) pose a high risk to the environment and health[30]. Biomimetic approaches for the synthesis of silica would be able to reduce the environmental impact of silica synthesis, and provide potential economic advantages by reducing and/or eliminating the need for organic solvents, reducing wastes and simplifying processes by using less reagents and water-based chemistries[31].

Natural silica is found in plants as phytoliths and also utilized in certain animals. These applications of silica are of great scientific interest because of the degree of structural sophistication achieved through this kind of bottom-up processes.

Diatoms are model organisms for studying biomineralization processes[32,33]. Nanofabrication of silica in diatoms occurs under ambient conditions at slightly acidic pH, and results from specific interactions between silicic acid derivatives and cationically charged proteins called silaffins[34,35], or long chain polyamines. It has been demonstrated that these biomolecules are able to induce rapid silica condensation in vitro[36], exercising the same role of the cationic surfactants in Stöber processes.

The choice of silica as mimicking scaffold of titania for the set-up of a composite catalyst is driven by the fact that they share the same structure and chemical properties, but ^{29}Si is much easier to be analyzed through magnetic resonance than $^{47/49}$Ti, having greater sensitivity ($\gamma = -8.47\,\mathrm{MHz\,T^{-1}}$) and being not quadrupolar ($I = 1/2$).

1.4 Lysozyme

In this thesis work, the templating biomolecule for the synthesis of both SiO_2 and TiO_2 nanoparticles is lysozyme, a small prolate protein present in many animal organisms (figure 1.7). It is found in relevant concentrations in human secretions, like tears and saliva, and in hen egg, because it has a mild bactericidal activity.

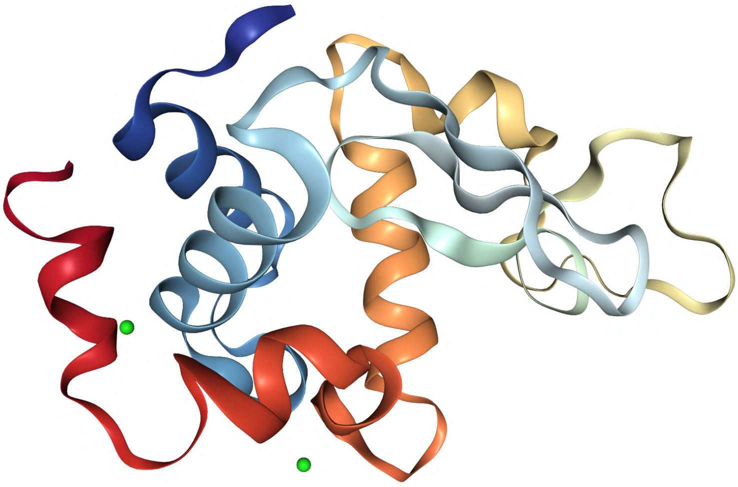

Figure 1.7: Structure of hen-egg lysozyme, obtained by X-ray diffraction. PDB: 1DPX[37]

Its primary structure consists of 149 aminoacids (molecular weight: 14.4 kDa), organized in two domains and distributed as shown in figure 1.8a.

When lysozyme folds, the hydrophobic aminoacids bury inside the protein core, leaving a marked positive charge on the surface. Comparing lysozyme primary structure with the average distribution of aminoacids in soluble proteins (figure 1.8b), it appears clear that this lysozyme feature is quite unusual, since generally proteins exhibit an overall negative charge on the surface. In fact lysozyme exhibits much less negative residues with respect to the average.

This peculiarity is the main reason of the antibacterial activity of lysozyme in vivo: it is able to favour the phagocitosis of bacteria reducing their negative surface charge through electrostatic interactions, and prompts the hydrolysis of the peptidoglycans in gram-positive bacteria.

The best choice for the set-up of a catalytic device able to perform oxidation reactions of organic molecules would be cytochrome-c. The main difficulty in the employment of cytochrome-c is the characterization through solid state NMR of a composite containing it, because the presence of a paramagnetic iron atom would be cause of several complications in the spectra, such as paramagnetic relaxation enhancement and paramagnetic chemical shifts.

Lysozyme can be used to simulate the behaviour of cytochrome-c in a composite catalyst of this kind, because it has the same mass and the same surface charge of cytochrome-c, but being diamagnetic it is much easier to be studied through magnetic resonance techniques.

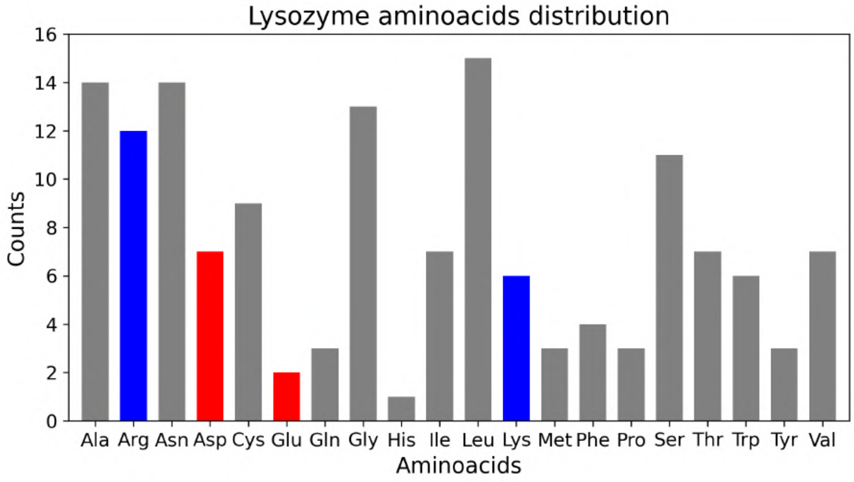

(a) Lysozyme aminoacids distribution

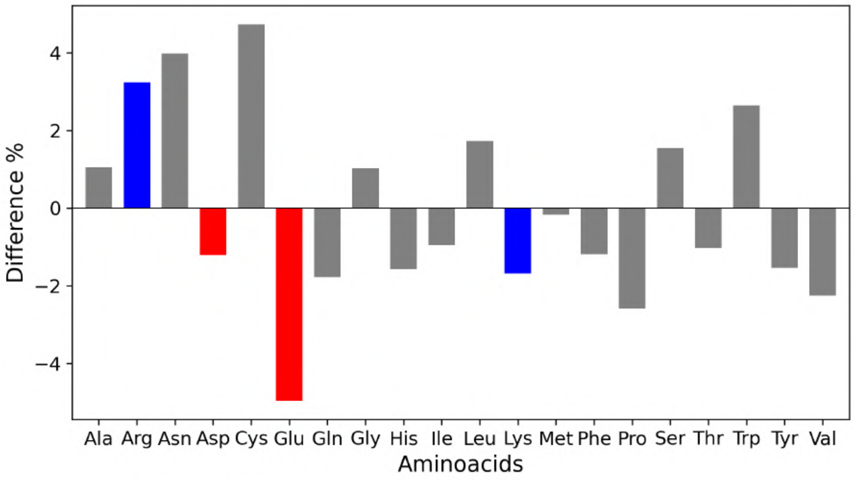

(b) Difference with average distribution

Figure 1.8: (**a**) Representative bar-plot of the aminoacids distribution in the primary structure of lysozyme.
(**b**) Amino acid compositional difference between lysozyme and average globular soluble proteins. Hydrophobic residues are shown in grey, positively charged residues in blue, negatively charged residues in red.

2. Experimental part

Among the different bioinspired silica preparation strategies, the bioinspired sol-gel synthesis proposed by Luckarift et al.[38] is quite convenient. The preparation is based on inexpensive and readily available reagents, is fast, can be performed at ambient conditions (i.e. room temperature and atmosphere), and yields a condensed silica network without thermal processing. Notably, titania can be produced through a very similar chemistry.

2.1 Preparation of the samples

Hen-egg lysozyme, tetramethylorthosilicate (TMOS, 98% pure) and titanium bis-ammonium lactate dihydrate (TiBALDH, 2 mol dm^{-3} stock solution) were purchased from Sigma-Aldrich and used without further purification.

2.1.1 lys-SiO_2

A stock solution of lysozyme 100 mg cm^{-3} in MilliQ water has been prepared. TMOS was hydrolyzed in 1 mmol dm^{-3} HCl solution, obtaining a 1 mol dm^{-3} final concentration. The precipitation mixture consisted of buffer (TRIS pH 8.5, 80%), hydrolyzed TMOS (final concentration 100 mmol dm^{-3}, 10%) and lysozyme (final concentration 10 mg cm^{-3}, 10%). The presence of a white colloidal precipitate has been observed after a few second from the mixing of the solutions. The mixture was stirred at room temperature for 5 minutes, then the resultant particles were removed by centrifugation at 14 000 g for 10 minutes and washed three times with MilliQ water.

In order to assess the behaviour and the characteristics of the composite when the protein is denaturated, part of the nanoparticles were washed either with guanidinium chloride (GnHCl, 6 mol dm^{-3}) and dithiotreitol (DTT, 10 mmol dm^{-3}) or urea ($CO(NH_2)_2$, 6 mol dm^{-3}) and dithiotreitol (DTT, 10 mmol dm^{-3}), then washed other three times with water before lyophylization. These samples will be named GnHCl and urea, respectively.

Another aliquot of nanoparticles have been washed with D_2O in order to discriminate among the accessible and non-accessible protons to the solvent. To do so, the sample has been freeze-dried and subsequently rehydrated with D_2O, for two times. This sample will be referred to as D_2O.

A scheme of the samples preparation is reported in table 2.1.

To provide a metal functionalization in the composite structure, the starting solution of precursors were prepared dissolving either lysozyme or TMOS in salt solutions of different transition metals. The chosen cations were V(+5), Co(2+)

Sample	Washing solution	Procedure
lys-SiO_2	Water	– Washing with water 3×; – Freeze drying.
lys-SiO_2-D_2O	D_2O	– Washing with water 3×; – freeze-drying; – rehydration with D_2O; – freeze-drying; – rehydration with D_2O; – freeze-drying.
lys-SiO_2-GnHCl	GnHCl $6\,\mathrm{mol\,dm^{-3}}$, DTT $10\,\mathrm{mmol\,dm^{-3}}$	– Washing with water 3×; – washing with GnHCl and DTT solution; – washing with water 3×; – freeze-drying.
lys-SiO_2-urea	Urea $6\,\mathrm{mol\,dm^{-3}}$, DTT $10\,\mathrm{mmol\,dm^{-3}}$	– Washing with water 3×; – washing with urea and DTT solution; – washing with water 3×; – freeze-drying.
lys-SiO_2-NaCl	NaCl $1\,\mathrm{mol\,dm^{-3}}$	– Washing with water 3×; – washing with NaCl; – washing with water 3×; – freeze drying.

Table 2.1: Resume table of the samples treated in different conditions.

and Cu(2+), therefore sodium orthovanadate, cobalt(II) acetate and copper(II) acetate were employed, respectively. The concentrations of the solutions have been chosen in order to obtain a metal to silicon mole ratio of 5%, 1% and 0.5% in the final composite, as shown in table 2.2.

Sample	[Si] mmol dm^{-3}	[lys] mg cm^{-3}	[Metal] mmol dm^{-3}
lys-SiO_2	100	10	–
lys-SiO_2-V 5%	100	10	5
lys-SiO_2-V 1%	100	10	1
lys-SiO_2-V 0.5%	100	10	0.5
lys-SiO_2-Co 5%	100	10	5
lys-SiO_2-Co 1%	100	10	1
lys-SiO_2-Co 0.5%	100	10	0.5
lys-SiO_2-Cu 5%	100	10	5
lys-SiO_2-Cu 1%	100	10	1
lys-SiO_2-Cu 0.5%	100	10	0.5

Table 2.2: Summary table showing the concentrations of the various components in all silica-lysozyme composites.

2.1.2 lys-TiO_2

The same protocol has been followed for the preparation of the TiO_2 composite. A solution of TiBALDH in water (1 mmol dm^{-3}) took the place of the stock TMOS solution, and has been used in the same way as shown in the aforementioned scheme.

GnHCl and urea samples were prepared in this case, too.

The lys-TiO_2 composite has been immobilized on the surface on an indium-tin oxide (ITO) electrode, in order to analyse the photochemical activity of titania. On a glass slide covered with ITO, 50 mm^3 of 100 mg cm^{-3} lysozyme solution and 50 mm^3 of 100 mmol dm^{-3} TiBALDH solution have been deposited to form a droplet. After drying overnight, the gelly spot was sintered in muffle oven at 500 °C for 30 minutes in order to achieve the immobilization of titania and to eliminate residual water and lysozyme from the electrode surface. This step should also cause the interconversion of TiO_2 from amorphous to anatase.

2.2 Instrumentation

2.2.1 Scanning Electron Microscopy

All the samples were investigated by a ΣIGMA high-resolution scanning electron microscope (SEM, Carl Zeiss) based on the GEMINI column which features a high-brightness Schottky field emission source beam booster and in-lens secondary electron detector. Measurements were performed on uncoated samples with an acceleration potential of 2 kV and at a working distance of about 4 mm.

2.2.2 Solid State NMR

Solid state NMR experiments were recorded on a Bruker Avance II spectrometer operating at 700 MHz ^{1}H Larmor frequency (16.4 T), corresponding to 139 MHz ^{29}Si Larmor frequency and 176 MHz ^{13}C Larmor frequency. The spectrometer is equipped with a 3.2 BVT MAS probehead in double resonance mode.

All powder samples were loaded into a 3.2 mm zirconium oxide rotor and spinned at 11 kHz of MAS frequency.

The 90° pulse duration on ^{29}Si and ^{13}C for all the analyzed samples were set to 7.5 µs and 3.5 µs respectively. The durations of 90° pulse on ^{1}H in the different samples are shown in table 2.3.

The monodimensional ^{29}Si spectra in direct excitation were acquired with CPMG echo train pulse sequence, and then the 24 echoes were separated. Only the first decay has been taken as quantitatively relevant, because the transverse relaxation times are different for the different silicon sites. Interscan delays were set to three times the ^{29}Si T_1 of the slowest-relaxing species (Q^4), in order to make the experiments quantitative.

For the bidimensional $\{^1H\}$-^{13}C and $\{^1H\}$-^{29}Si HETCOR experiments, cross-polarization was achieved by matching the $k = 1$ Hartmann-Hahn condition. The spectral windows for the different nuclei were 60, 248 and 249 ppm for ^{1}H, ^{13}C and ^{29}Si , respectively. During the ^{1}H magnetization evolution under the chemical shift in the indirect dimension of heteronuclear correlation experiments, the PMLG decoupling sequence was used to suppress ^{1}H -^{1}H dipolar couplings. In these experiments, interscan delay was set to 1.3 T_1 of the ^{1}H relaxation time, as reported in table 2.4. CPMG echo-train acquisition has been employed also for $\{^1H\}$-^{29}Si HETCOR in the direct dimension, and the 24 echoes were co-added. These spectra have been denoised using Multivariate Curve Resolution on the data in the time domain[39]. The same window function as the monodimensional spectra has been employed for both dimensions.

The monodimensional ^{29}Si spectra were processed imposing a squared-sine window function according to equation 2.1, where AQ is the number of points of the FID and SSB has been set to 2.

$$\mathrm{QSINE}(t) = \sin\left[\left(\pi - \frac{\pi}{\mathrm{SSB}}\right)\frac{t}{\mathrm{AQ}} + \frac{\pi}{\mathrm{SSB}}\right]^2 \qquad t \in [0, \mathrm{AQ}] \tag{2.1}$$

Freeze-dried sample	Rehydrated with H_2O	Rehydrated with D_2O	Washed with GnHCl	Washed with NaCl
2.90	2.90	3.17	2.97	3.17

Table 2.3: Duration of the ^{1}H 90° pulse in HETCOR experiments, in µs.

2.2.3 Electrochemical measurements

The photocurrent measurements were performed in 0.1 mol dm^{-3} KCl solution in MilliQ water, starting from the salt purchased from Sigma Aldrich without further purification.

Freeze-dried sample	Rehydrated with H_2O	Rehydrated with D_2O	Washed with GnHCl	Washed with NaCl
3.0	2.5	0.8	0.8	3.0

Table 2.4: Interscan delay in HETCOR experiments, in s.

The experimental setup was equipped with a three electrodes system. In particular, an Ag/AgCl pseudo-reference electrode (RE) constituted by a a silver thread has been used. A platinum thread, used as counterelectrode (CE), closed the circuit. Ultimately, as working electrode (WE), i.e. the electrode on whose surface happens the redox reaction, a transparent conductive substrate based on indium(III) oxide and tin(IV) oxide (indium-tin oxide, *ITO*) has been employed.

These electrodes were connected to a Metrohm Autolab PGSTAT10 potentiostat/galvanostat. The linkage with the WE was achieved through an adhesive conductive copper strip, positioned on the ITO layer.

The electrodes and the electrolytic solution (KCl, $0.1\,\mathrm{mol\,dm^{-3}}$) were placed in a sectioned truncated conical structure carved inside a polymethylmetacrilate cell. Between the two cylindrical sections which constitute that cell, securely jointed by metallic screws, the ITO/TiO_2 electrode under examination is inserted. The upper part of the cell, in central position, presents a rubber *o-ring*, that seals the electrode surface keeping the analyzed area constant.

The electrode surface is irradiated using a Camag UV lamp, centered at 366 nm

In the amperometric measurements, the potential has been set at a constant value and the resulting current has been monitored over time. The UV light has been turned on and off in order to observe the variation in the current in different conditions.

The data have been acquired and processed using the NOVA software from Metrohm Autolab.

3. Results and discussion

3.1 Preliminary results

The entrapment of cyt-c and lysozyme inside TiO_2 was achieved following the protocol given in[38]. The precipitation mixture was prepared by mixing 100 mm^3 of 10 mg cm^{-3} of either cyt-c or lysozyme solution with 20 mm^3 of 25% w/v TiBALDH solution. The formation of a precipitate is apparent in both cases (figure 3.1).

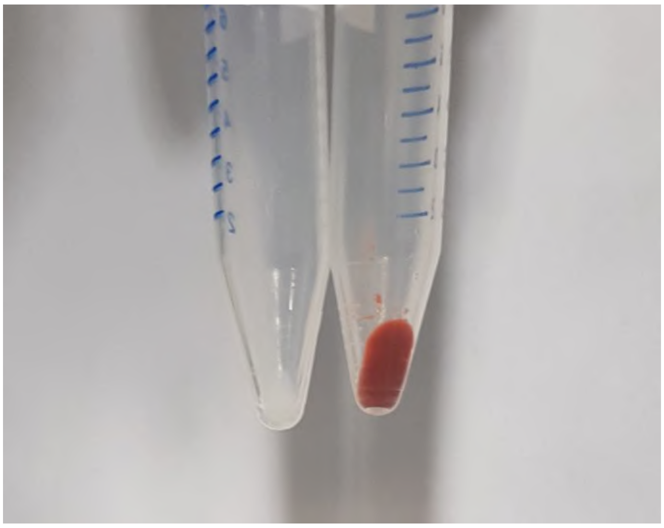

Figure 3.1: Titanium dioxide composites formed in the presence of cyt-c (right) and lysozyme (left).

Given the relatively high cyt-c loading in the composites, it is possible to acquire solid-state NMR spectra of the immobilized cyt-c. The spectrum maps almost completely with the spectrum of the free protein (figure 3.2).

3.1.1 Measurements of cyt-c in solution

The so-synthesized cyt-c-biotitania composite was characterized via cyclic voltammetry using carbon based screen-printed electrochemical cells (Drop-sens). To this end one aliquot was thaw and the protein was diluted to 100 µmol dm^{-3} in phosphate buffer solution, then 60 mm^3 of the obtained solution was dropped on the electrochemical strip. The voltammograms are shown in figure 3.3.

No significant signal was observed when CV measurement were recorded using buffer (figure 3.3a). On the contrary, when a solution containing cyt-c was analyzed, it was possible to observe a peak at around 0.2 V, that can be attributed

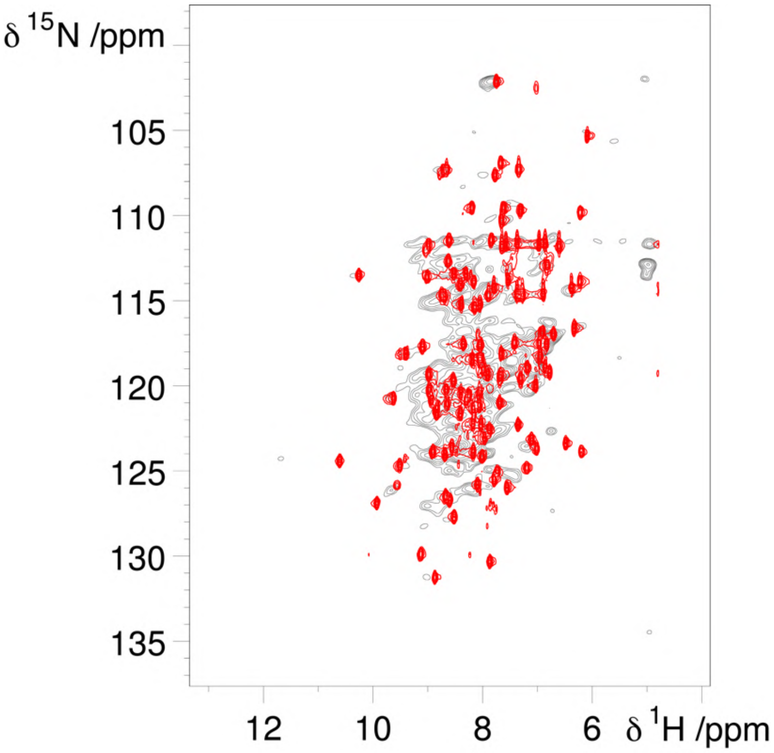

Figure 3.2: ^{1}H-^{15}N HSQC spectrum of the free protein (red) superimposed to the ^{1}H-detected ^{1}H-^{15}N HETCOR spectrum acquired in the solid state (black). The HETCOR spectrum has been acquired at 850 MHz proton Larmor frequency, and the sample has been spinned at 60 kHz MAS frequency.

to the presence of the iron atoms in the active site of the protein; the intensity of this signal remained stable within successive scans. The signal due to the reduction of iron(III) was observed at around 0 V, but it was very weak. Moreover, two signals at around 0.6 V and 0.8 V were present in the first positive going scan and decreased in the successive runs. These electrochemical signals can probably be attributed to the oxidation of some functional groups present in the protein structure (i.e. NH_2).

In order to better characterize the electrochemical behavior of cyt-c, successive voltammetric scans at different scan rate were performed on the same SPCE; measurement were repeated in both direction of potential scan (figure 3.4).

The signal attributed to the presence of iron was observed in all the conditions used; i_{pa} intensity increased with the scan rate and a shift of the peak position was observed. On the contrary, the intensity of the broad reduction signal at around 0 V i_{pc} remained almost constant.

3.1.2 Measurements of cyt-c after encapsulation

The sample was made by dropping 10 mm^3 of the cyt-c-TiBALDH precipitation mixture, vortexed, onto the surface of the working electrode of a SPCE. The sensors were modified using the lysozyme-TiBALDH precipitation mixture in order to obtain the blank of our measurements (BlankLIZ). Other two SPCE were modified with the only mixtures of reagents in order to evaluate the possible effects of the sensor surface and the interaction with ink constituents (Blank). The

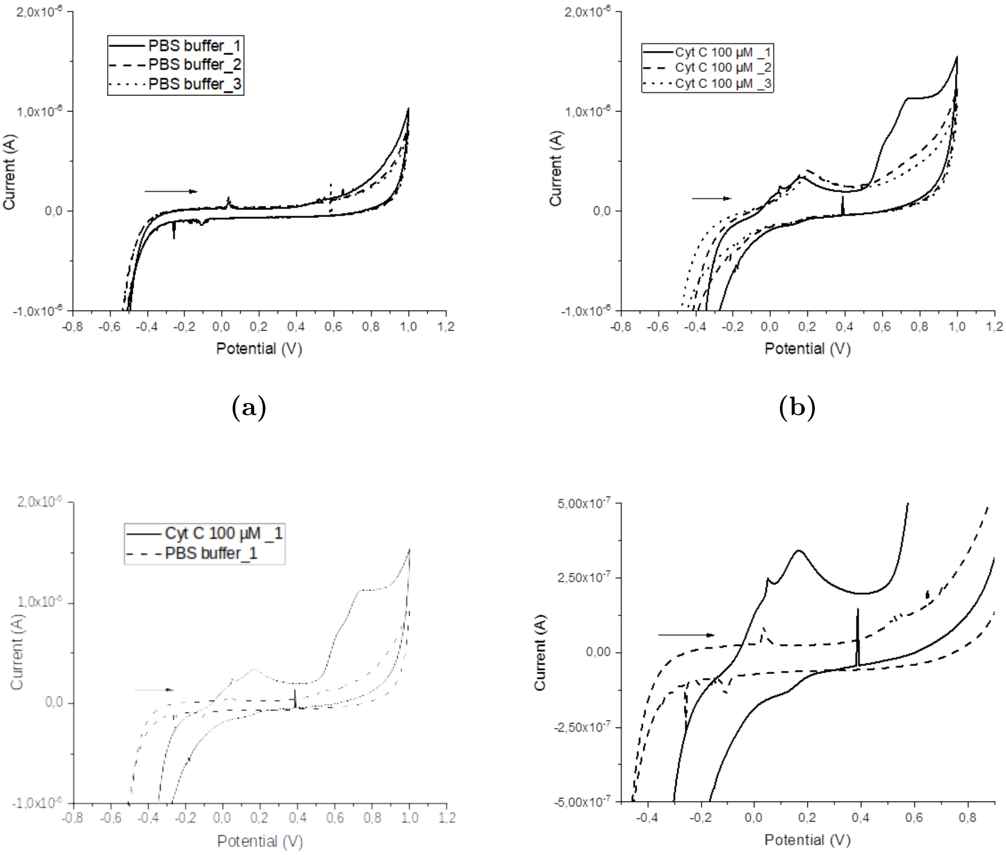

(a) **(b)**

(c) **(d)**

Figure 3.3: Three consecutive voltammetric scans of PBS buffer (**a**) and cyt-c 100 µmol dm^{-3} in PBS buffer (**b**). In graph **c** the comparison between the first scan recorded at SPCE (Dropsens) of buffer and the first scan of cyt-c 100 µmol dm^{-3} solution was reported (Scan rate 50 mV s^{-1}). **d**: insert of graph **c**.

obtained modified SPCE were used to perform electrochemical characterization, using PBS as supporting electrolyte.

In figure 3.5a and 3.5b the three repetition of CV obtained at Ti-BALDH/cyt-c SPCE were reported; both scanning direction were reported, at a scan rate of 50 mV s^{-1}. Repetitive scans seemed to cause a sort of activation of the electrode surface; thus in the successive scans recorded at 10 mV s^{-1}, a weak oxidation signal was obtained at around 0.2 V; a slight increase in the intensity was also observed (figure 3.6).

Thus a possible electrochemical detection of cyt-c can be achieved, with a discrimination between the signals obtained for TiBALDH/cyt-c SPCE and TiBALDH/lysozyme SPCE. When a sensor modified with the only mixtures of reagents was analyzed large current was obtained in repetitive scans; this behaviour can be attributed to the differences in the precipitation of TiBALDH at the electrode surface, in the absence of a protein (figure 3.7).

Different versions of the composite were tested in order to observe if the composite is actually able to catalyze oxidation reactions in a UV plate. The composite containing cyt-c is functional in oxidizing pyrogallol under sunlight

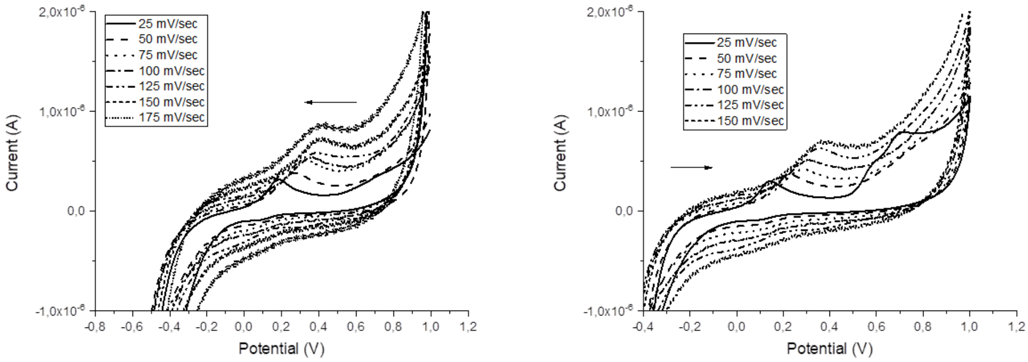

(a) **(b)**

Figure 3.4: Successive voltammetric scans of cyt-c 100 µmol dm^{-3} in PBS buffer; scan rate used were 25, 50, 75, 100, 125, 150 and 175 mV s^{-1}.

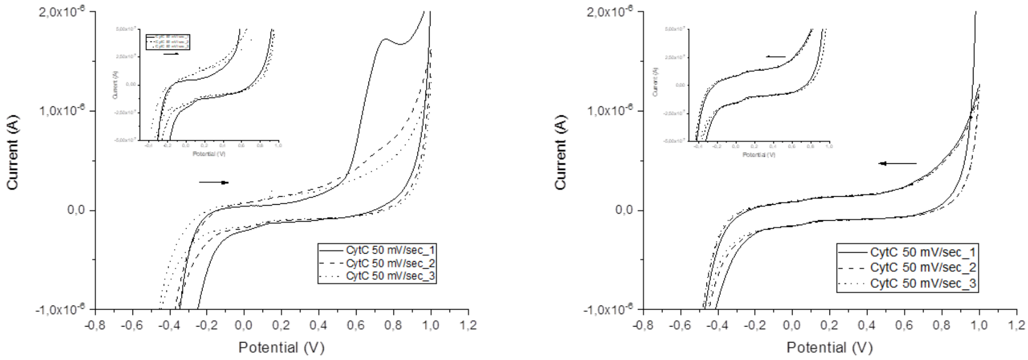

(a) **(b)**

Figure 3.5: Voltammetric scans obtained for TiBALDH/cyt-c SPCE with PBS buffer; scan rate 50 mV s^{-1}.

and/or artificial UV light irradiation. However, the oxidation does not proceed to the expected product (purpurogallin). Furthermore, it worths to note that the reaction happens also without the presence of cyt-c (figure 3.8).

In light of these results, it was needed to simplify the system in order to better investigate its properties.

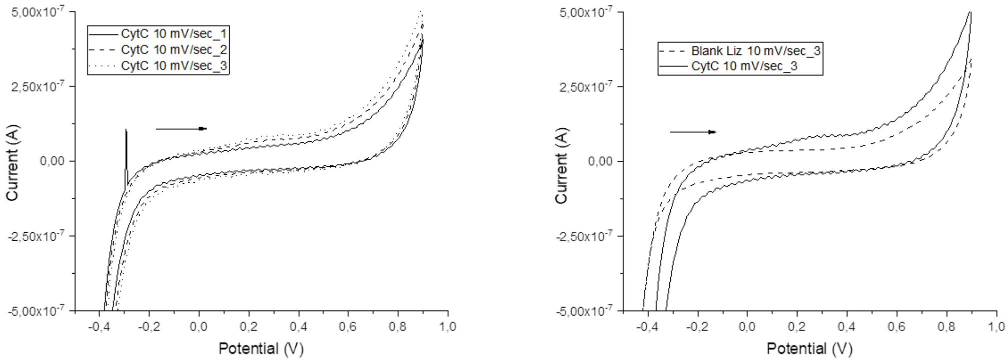

(a) **(b)**

Figure 3.6: Voltammetric scans obtained for TiBALDH/cyt-c SPCE with PBS buffer; scan rate 10 mV s^{-1}.

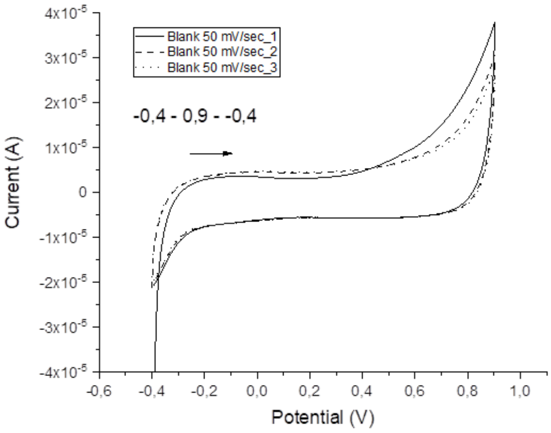

Figure 3.7: Voltammetric scans recorded at TiBALDH/SPCE.

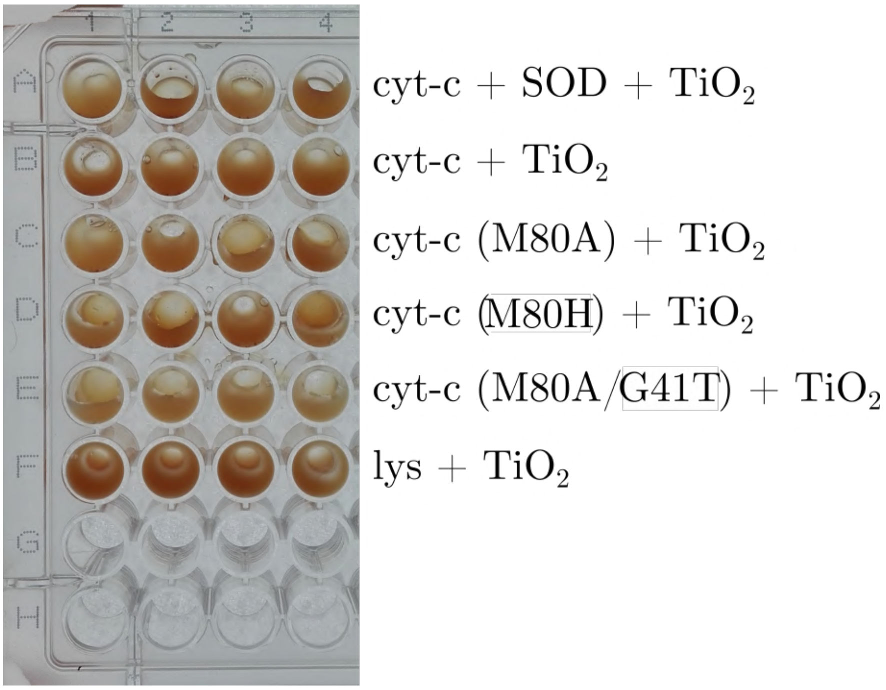

Figure 3.8: UV plate in which the catalytic tests on the composite were performed. In all wells of each row, from top to bottom: cyt-c + superoxide dismutase (*SOD*) + TiO_2, cyt-c + TiO_2, cyt-c mutant (M80A) + TiO_2, cyt-c mutant (m80h) + TiO_2, cyt-c mutant (M80A/d30R) + TiO_2, lys + TiO_2.

3.2 Morphology and chemical behaviour of the composite

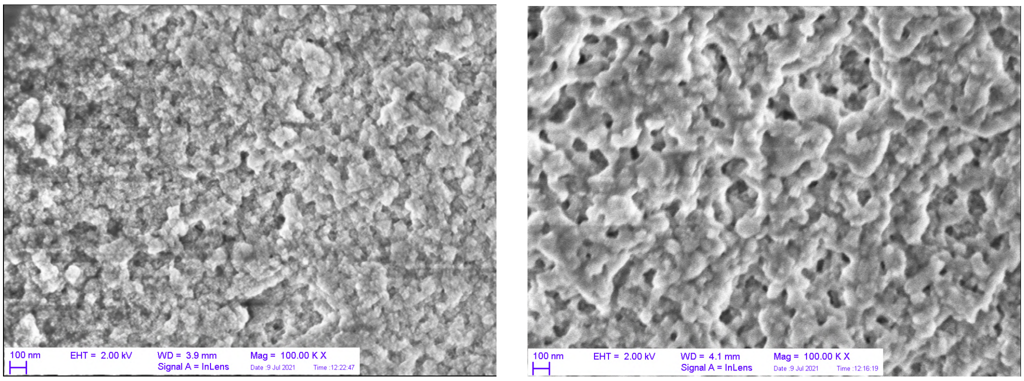

(a) EHT: 2 kV, mag: 100 kx
3.2 × 2.4 µm

(b) EHT: 2 kV, mag: 100 kx
3.6 × 2.7 µm

Figure 3.9: SEM images of lys-SiO_2 composite, freeze-dried (**a**) and washed with NaCl (**b**)

The obtained lys-SiO_2 composite, as can be seen from SEM images (figure 3.9), consists of spherical particles whose diameter is about 50 nm.

The SEM images of lys-TiO_2 composite, deposited on the ITO electrode surface, show homogeneous deposition of much smaller particles, around 10 nm of diameter (figure 3.10b). From the pictures at lower enlargement (figure 3.10a), several cracks about 3 µm wide are visible, whose formation may be because of the rupture of water surface tension during the evaporation of the solvent and heat-treating in muffle oven. However, the aforementioned deposit of TiO_2 nanoparticles is not broken or altered inside these cracks.

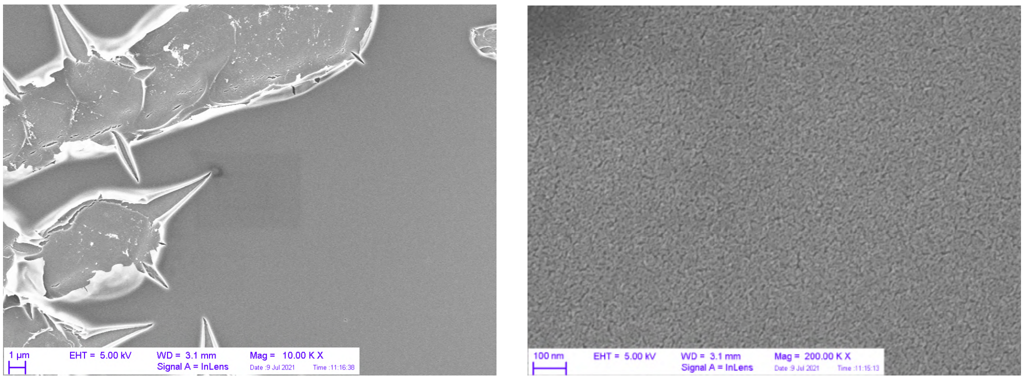

(a) EHT: 5 kV, mag: 10 kx
36 × 27 µm

(b) EHT: 5 kV, mag: 200 kx
1.6 × 1.2 µm

Figure 3.10: SEM images of lys-TiO_2 composite deposited on indium-tin oxide electrode surface.

According to the results presented in similar works[40–42], the possible relative arrangements of protein and silica inside the composite are:

1. the protein is trapped inside the silica particles by electrostatic interactions;
2. the protein has been trapped inside the silica particles during the formation and cannot exit, but marginal interactions exist;

3. the protein is interacting with the exterior of the silica particles via mainly electrostatic interactions.

These three arrangements should provide a distinct outcome for different treatments of the sample. The release of the protein has been quantified by UV-visible spectrometry, measuring the absorbance at $\lambda = 280\,\mathrm{nm}$ (molar extinction coefficient $\varepsilon = 36\,\mathrm{cm^2\,mmol^{-1}}$). The outcomes of this analysis are summarized in table 3.1.

Upon denaturation with either GnHCl or urea and reduction with DTT, the protein is quantitatively released, regardless of the ionic strength, leaving the silica structure practically unperturbed. Washing with NaCl causes the release of about 1/5 of the protein. Washings with water seem not to cause any release of lysozyme from the composite. These experimental observations suggest that the protein is found at least for the 20% interacting with the surface of the SiO_2 particles, whereas the remaining 80% may be trapped inside the silica network due to steric interactions.

Conditions	**Interaction models**			**Observed behaviour**
	Charge inside 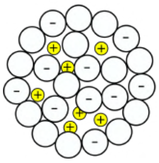	Steric inside 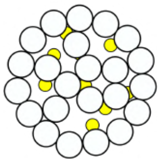	Charge outside 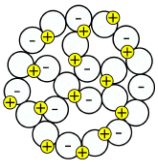	
Only water	Retained	Retained	Retained	Retained
GnHCl + DTT – denaturing + reducing, high ionic strength	Released	Released	Released	Released
Urea + DTT – denaturing + reducing, low ionic strength	Retained	Released	Retained	Released
NaCl – high ionic strength	Retained	Retained	Released	80% Retained 20% Released

Table 3.1: Behaviour of the lys-SiO_2 composite with respect to ionic strength and denaturation.

The same experiments were performed also on the lys-TiO_2 composite, with quite different results (table 3.2). Upon denaturation and reduction with GnHCl and DTT, only the 25% of the protein is released, whereas the presence of high ionic strength ($1\,\mathrm{mol\,dm^{-3}}$ NaCl) sorts no effects, as well as what happens with washings with water. These outcomes suggest a different relative arrangement of lysozyme and inorganic matrix in this composite with respect to the lys-SiO_2 one, that might be either a consequence of the different morphology of the material or of the existence of other interactions between the components.

Conditions	**Interaction models**			**Observed behaviour**
	Charge inside 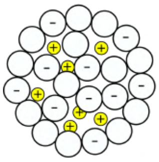	Steric inside 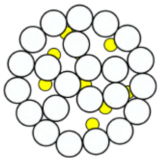	Charge outside 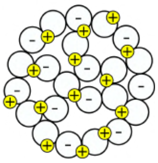	
Only water	Retained	Retained	Retained	Retained
GnHCl + DTT – denaturing + reducing, high ionic strength	Released	Released	Released	25% Released 75% Retained
NaCl – high ionic strength	Retained	Retained	Released	Retained

Table 3.2: Behaviour of the lys-TiO_2 composite with respect to ionic strength and denaturation.

3.3 ^{13}C –NMR spectra

The ^{13}C ssNMR spectra of the protein acquired on the freeze-dried sample, reported in figure 3.11, show low resolution due to structural heterogeneity, as typical for dry protein samples. However, upon rehydration with H_2O, the spectral resolution increases because of the water that promotes local dynamics within the protein This observation is rather common on passing from freeze-dried to rehydrated biomolecules[43–55].

Comparison with the spectrum of sedimented lysozyme shows that the broader envelope of the composite spectrum encompasses the frequency range that is observed for the sedimented protein. Since the spread of the ^{13}C NMR signals is a reporter of the folding of the protein, it can be inferred that the fold of the protein is preserved[56,57]. Even with a resulting broad spectrum, the distinctive features of the folded protein are observed, i.e. features from the methyl-bearing sidechains, which have shifts lower than 20 ppm when the hydrophobic core is intact, as well as in the overall distribution of the aliphatic region, that is 65 ppm to 5 ppm.

Of note, the peak around 157 ppm can be attributed to either arginine or tyrosine C_ζ. Since the lysozyme primary structure features 11 arginines and 3 tyrosines, most of the intensity of this peak can be attributed to arginine residues. The relative intensity of the peak in the composite with respect to the protein sediment can be attributed to a lower mobility of the sidechains in the composite with respect to the free protein. It can also be noted that this peak is markedly narrowed upon rehydration and, considering the high arginine content, this behaviour is similar to what observed for arginine ^{15}N in ubiquitin in MCM41[58].

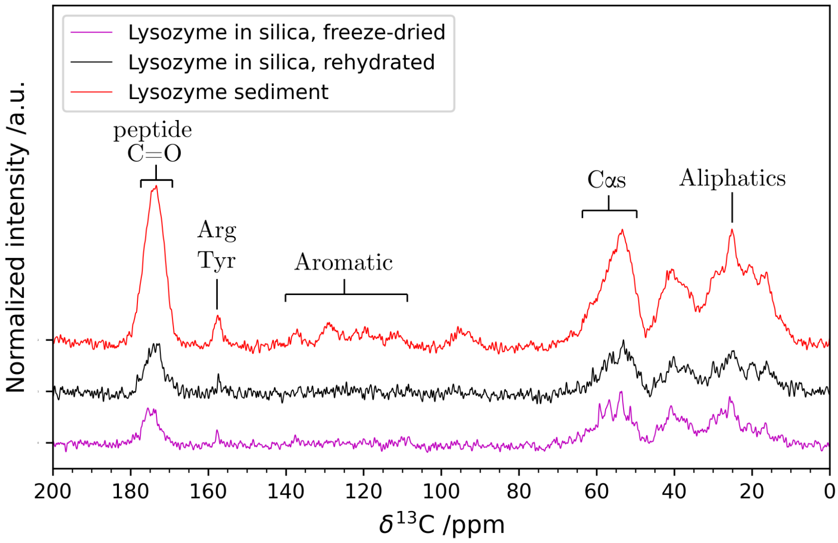

Figure 3.11: {^{1}H}-^{13}C cross-polarization ssNMR spectra of the composite (freeze-dried sample in red and rehydrated in black), and of lysozyme sediment (in magenta). The spectral regions where protein signals are usually observed are annotated on the figure.

3.4 ^{29}Si –NMR spectra

It is possible to characterize the silica matrix through ^{29}Si NMR. The ^{29}Si ssNMR spectrum of the freeze-dried composite, reported in figure 3.12 shows signals originating from siloxanes (Q^4, around −110 ppm), monosilanols (Q^3, around −100 ppm) and geminal silanols (Q^2, around −90 ppm, barely visible). The ratio between the intensities of Q^3 and Q^4 is indicative of silica condensation degree.

The spectrum has been deconvoluted with three gaussians employing the Levenberg-Marquardt algorithm for non-linear least squares optimization[59,60], implemented in the python package `lmfit`[61]. The chosen cost function to be optimized $f(\omega;\vec{k},\vec{\mu},\vec{\sigma}$ has been written as:

$$f(\omega;\vec{k},\vec{\mu},\vec{\sigma}) = S(\omega) - G(\omega;\vec{k},\vec{\mu},\vec{\sigma}) \tag{3.1}$$

$$G(\omega;\vec{k},\vec{\mu},\vec{\sigma}) = \sum_{i=1}^{3} \frac{k_i}{\sqrt{2\pi}\sigma_i} \exp\left[\frac{1}{2}\left(\frac{\omega-\mu_i}{\sigma_i}\right)^2\right] \tag{3.2}$$

$$\vec{k} = \begin{pmatrix} k_1 & k_2 & k_3 \end{pmatrix} \qquad \vec{\mu} = \begin{pmatrix} \mu_1 & \mu_2 & \mu_3 \end{pmatrix} \qquad \vec{\sigma} = \begin{pmatrix} \sigma_1 & \sigma_2 & \sigma_3 \end{pmatrix} \tag{3.3}$$

where the vectors $\vec{k},\vec{\mu},\vec{\sigma}$ contain the parameters of the gaussians that have to be optimized, i.e. integrals, central frequencies and standard deviations, respectively. For this procedure, the Fourier transform of later echoes of CPMG acquisition sequence have been employed to get a better estimation of the chemical shifts and linewidths of the signals. The optimized parameters got as result of the fitting are reported in table 3.3.

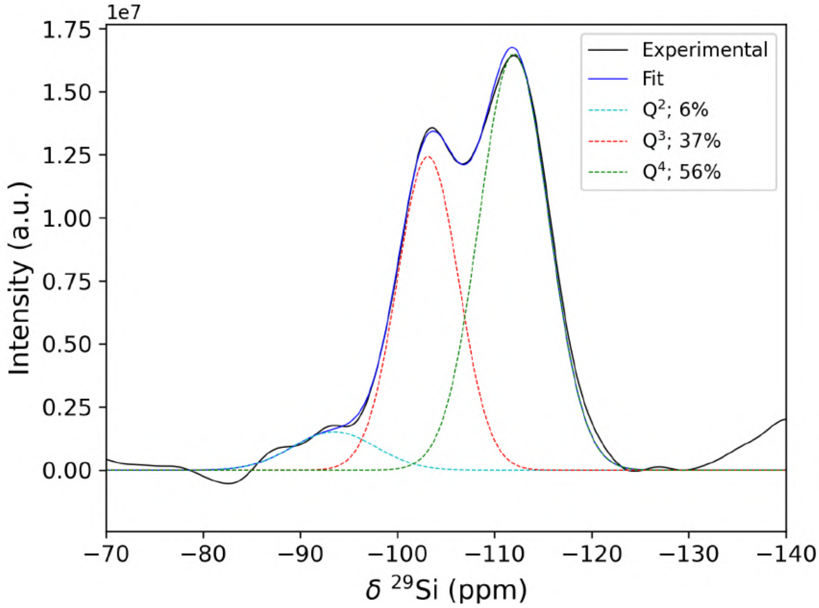

Figure 3.12: ^{29}Si direct excitation solid state NMR spectrum of the freeze-dried composite. The signal has been deconvoluted using three gaussians corresponding to Q^2, Q^3 and Q^4 sites.

Site	δ **/ppm**	σ **/Hz**	**Relative intensity**
Q^2	93.5	3004	6.2%
Q^3	103.1	2216	37.5%
Q^4	112.0	2509	56.3%

Table 3.3: Parameters of the gaussians that fit the direct excitation ^{29}Si spectrum of the freeze-dried composite.

The condensation degree of silica in this composite is 1.50, which is similar to the values observed for PL-12 silica (1.54), catMMP12/R5 and SBA-15 silica (1.6)[62,63]. Notably, silica gel obtained under the same conditions but without the protein (i.e. by natural condensation of hydrolyzed TMOS) has a Q^3/Q^4 ratio of 0.68 (figure 3.13, table 3.4), therefore is much less condensed. This is thought to be because of the electrostatic interaction that subsist between protein and precursor during the formation of the silica network, that allow the condensation of Si units in closer proximity one to each other respect to what happens in protein-free conditions.

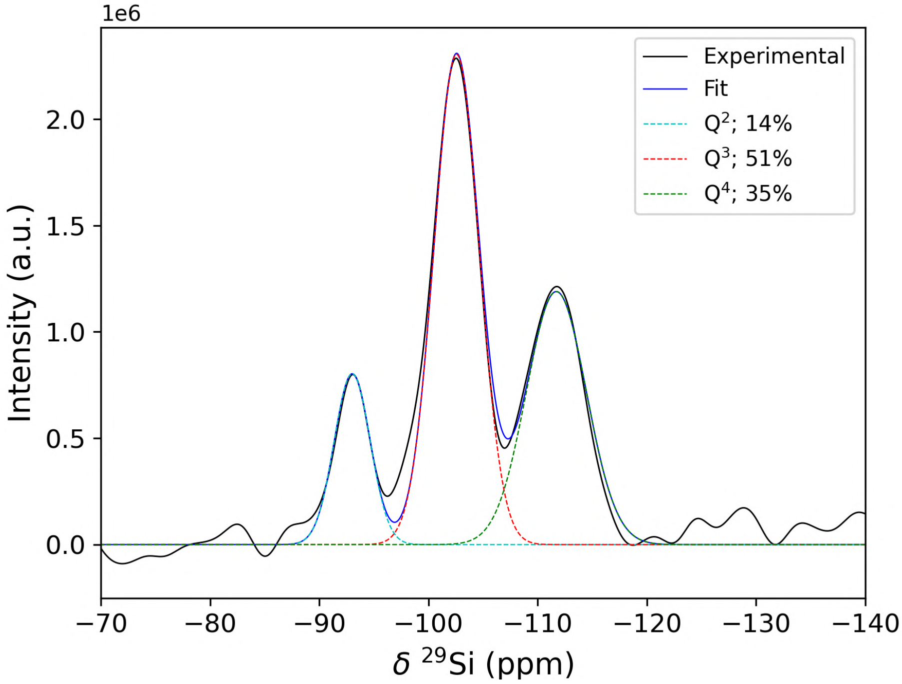

Figure 3.13: ^{29}Si direct excitation ssNMR spectrum of silica obtained through condensation of the precursor without the protein. The signal has been deconvoluted using three gaussians corresponding to Q^2, Q^3 and Q^4 sites.

Site	**δ /ppm**	**σ /Hz**	**Relative intensity**
Q^2	93.0	1155	14.1%
Q^3	102.6	1454	51.1%
Q^4	111.7	1921	34.8%

Table 3.4: Parameters of the gaussians that fit the direct excitation ^{29}Si spectrum of freeze-dried silica gel obtained without the presence of lysozyme.

The spectrum of the composite treated with GnHCl and DTT (figure 3.14, table 3.5) shows an increase of Q^3/Q^4 ratio to 1.72. This may be a consequence of the fact that lysozyme, when leaving the composite because of its denaturation, causes the detachment of the less condensed and more weakly bound silica parts. Furthermore, the SEM image of the sample washed with GnHCl and DTT looks more porous than the freeze-dried and washed with NaCl samples (figure 3.15).

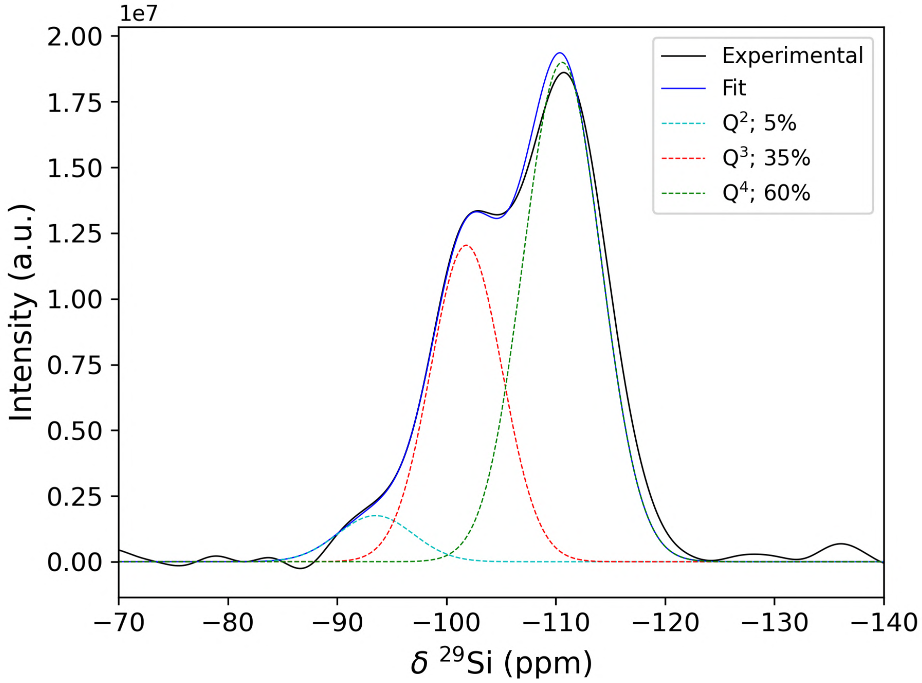

Figure 3.14: ^{29}Si direct excitation ssNMR spectrum of the composite treated with GnHCl and DTT. The signal has been deconvoluted using three gaussians corresponding to Q^2, Q^3 and Q^4 sites.

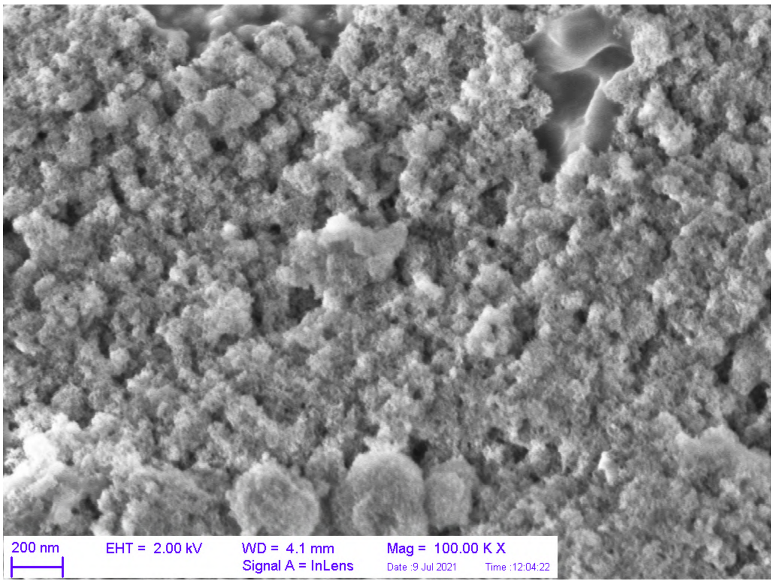

Figure 3.15: EHT: 2 kV, mag: 100 kx, 3.6 × 2.7 µm
SEM image of lys-SiO_2 composite washed with GnHCl and DTT.

Site	δ /ppm	σ /Hz	Relative intensity
Q^2	-93.5	2409	5.3%
Q^3	101.8	2297	34.8%
Q^4	110.6	2501	59.8%

Table 3.5: Parameters of the gaussians that fit the direct excitation ^{29}Si spectrum of freeze-dried composite treated with GnHCl and DTT, in order to denaturate the protein.

3.5 2D HETCOR spectra

A direct correlation of ^{13}C signals from the protein to ^{29}Si signals from the matrix would be able to reveal an intimate contact between the two components[64,65]. However, such correlation is necessarily limited since both the protein and the silica are in natural abundance (1.1% ^{13}C, 4.7% ^{29}Si) in the complex, reducing the probability of a coupled ^{13}C$-$^{29}Si pair to 1 in 2000[64]. Therefore, we decided to work on the comparison of the ^{1}H traces extracted from ^{1}H$-$X 2D correlation spectra (X being either ^{13}C or ^{29}Si), and to discriminate among the protons that act as polarization sources for the heteronuclear sites (figure 3.16).

The ^{1}H traces are obtained projecting the 2D HETCOR along the heteronucleus dimension in the regions shown in figure 3.17.

The proton spectra that are obtained projecting the 2D HETCOR of the dry sample along the ^{29}Si dimension show cross-polarization coming from at least three ^{1}H sources. All the traces are rather broad, with features around 1, 4 and 7 ppm. The first two are consistent with signals usually observed for silica: they can be attributed to silanols and physisorbed water respectively[66,67]. In biosilica, the feature around 1 ppm has also been ascribed to aliphatic protons from biomolecules[64]. The feature around 7 ppm is also sometimes observed in ^{1}H NMR spectra of silica and may arise from either $-\mathrm{OH_2}^+$ species or hydrogen-bonded silanols[67–69], water molecules hydrogen-bonded to bridging oxygen atoms[67,70] or, in the case of biosilica, from protein backbone and/or sidechains, although this latter assignment remains elusive[64].

Interestingly, in the spectrum of the gel obtained in the absence of lysozyme the 7 ppm and 1 ppm features are absent (figure 3.18).

One possibility to sort the assignment out is to find out whether the carbon nuclei in the protein and the silicon nuclei in the silica matrix are getting polarized

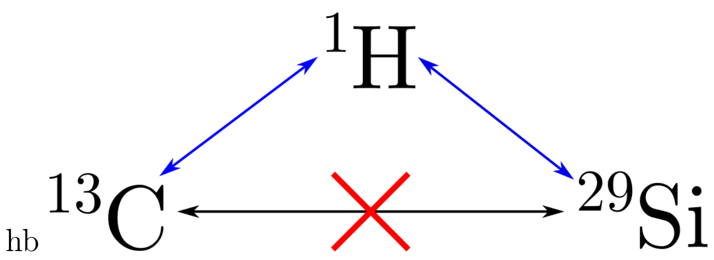

Figure 3.16: Since the acquisition of a direct ^{13}C $-$^{29}Si correlation spectra would be impossible, we decided to study the interaction between silica matrix and protein through the ^{1}H traces extracted from {^{1}H}-^{13}C and {^{1}H}-^{29}Si HETCOR spectra.

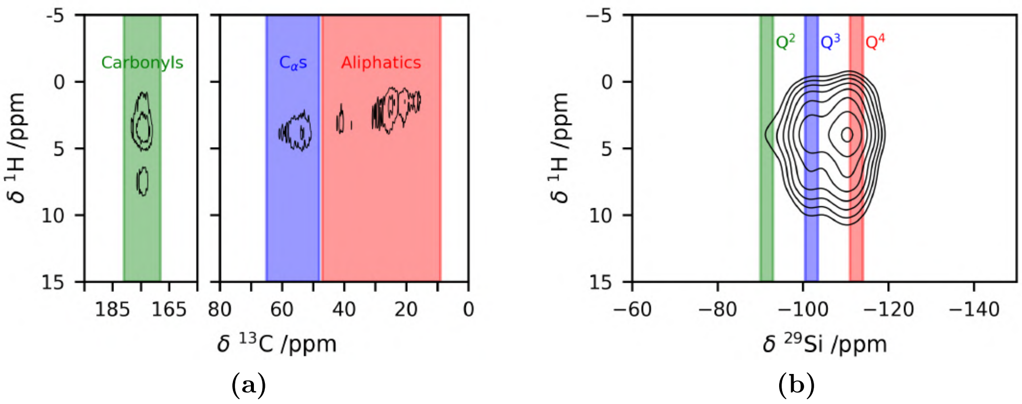

Figure 3.17: Integration range for ^{1}H traces over ^{13}C dimension in {^{1}H}-^{13}C spectra (**a**) and over ^{29}Si dimension in {^{1}H}-^{29}Si spectra (**b**). The assignment of the signals are annotated on the figures.

by the same proton sources or not. The {^{1}H}-^{13}C correlation spectra are common for a protein sample where maximal transfer is observed at the shorter mixing time of 150 µs for the directly bonded ^{1}H—^{13}C spin pairs, such as alpha protons (H_α) and alpha carbons (C_α), and at longer times for carbonyl carbons (C') polarized by amide protons (H_N) and H_α. A representative high resolution ^{1}H −NMR spectrum of lysozyme in solution is given alongside with the ^{1}H traces from the {^{1}H}-^{13}C HETCOR (figure 3.19).

In the {^{1}H}-^{29}Si HETCOR (integration regions are shown in figure 3.17b), Q^4 ^{29}Si sites receive magnetization mainly from silanols, whereas Q^3 ^{29}Si sites also receive magnetization from the protons downfield. When longer mixings are used, the contribution from this proton pool to the Q^4 sites increases (figure 3.20). The downfield proton pool is broad and overlaps with the H_N proton pool, as obtained from {^{1}H}-^{13}C HETCOR (figure 3.22).

If D_2O is used for rehydration, the ^{1}H peak corresponding to amides is lowered in the traces of ^{13}C spectra, but not abolished (figure 3.21). Interestingly, the downfield proton pool as detected from the {^{1}H}-^{29}Si HETCOR sharpens, and the overlap to the H_N proton from the {^{1}H}-^{13}C HETCOR becomes more apparent (figure 3.23).

Collectively, these observation seem to suggest that magnetization is transferred from either aromatic sidechains, from backbone amides, or from the amine and guanidino sidechains of lysine and arginine residues. However, other peaks at lower frequency in the ^{1}H dimension, which would be given by Q^4-Kε signals, are not observed, unlike other silica-peptide preparations, where clear indication of covalent interaction has been provided[64]. Therefore, we find a non-covalent interaction in this silica-lysozyme composite.

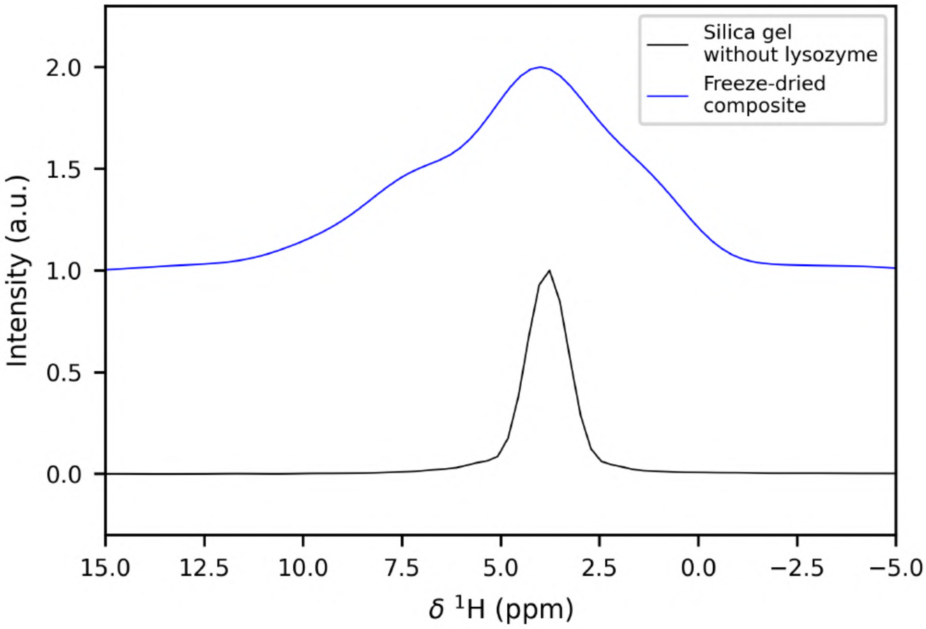

Figure 3.18: ^{1}H trace of the $\{^1H\}$-^{29}Si spectrum acquired with 10 ms of cross-polarization contact time on the freeze-dried silica gel obtained without lysozyme.

$\{^1H\}$-^{29}Si site	**Short** τ_{CP} δ /ppm	σ /Hz	Relative intensity	**Long** τ_{CP} δ /ppm	σ /Hz	Relative intensity
1	6.6	1403	44%	6.6	1446	43%
2	4.0	797	32%	4.0	767	29%
3	1.8	914	24%	1.8	978	28%
$\{^1H\}$-^{13}C site	δ /ppm	σ /Hz	Relative intensity	δ /ppm	σ /Hz	Relative intensity
1	7.6	816	40%	7.6	842	30%
2	3.9	654	52%	3.9	603	41%
3	1.9	684	8%	1.9	718	29%

Table 3.6: Parameters of the gaussians that fit the spectra in figure 3.22.

$\{^1H\}$-^{29}Si site	δ /ppm	σ /Hz	Relative intensity
1	7.3	1013	22%
2	4.5	787	33%
3	1.3	1068	45%
$\{^1H\}$-^{13}C site	δ /ppm	σ /Hz	Relative intensity
1	7.0	1019	21%
2	4.5	574	64%
3	1.6	523	15%

Table 3.7: Parameters of the gaussians that fit the spectra in figure 3.23.

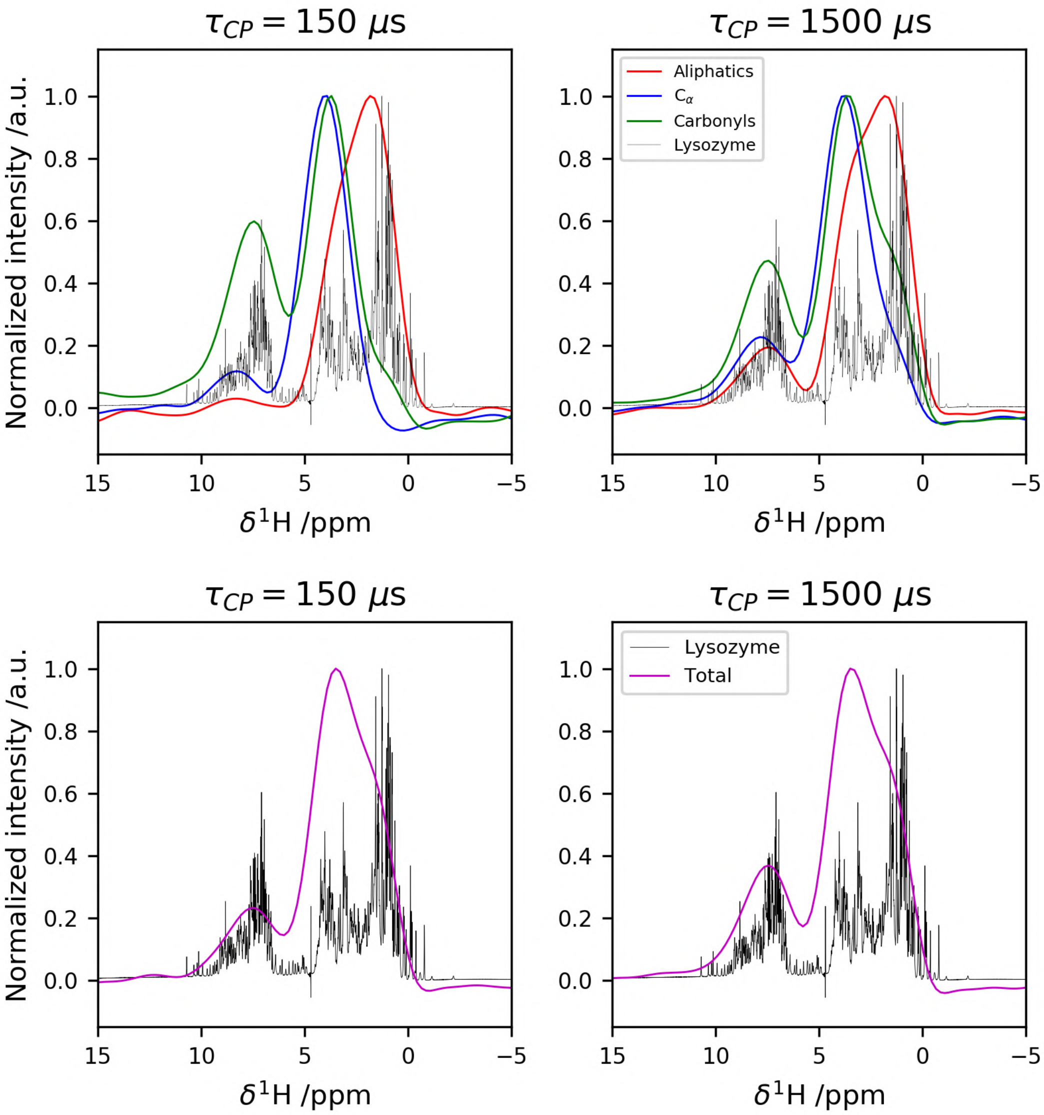

Figure 3.19: ^{1}H trace of the {^{1}H}-^{13}C HETCOR acquired with 150 µs (left) and 1.5 ms of cross-polarization contact time (right). In the top panel, the individual contribution of aliphatics (red), C$_\alpha$s (blue) and C' are reported. The integration ranges for the three groups is shown in figure 3.17a. In the bottom panels, the signal is integrated over all ^{13}C species. The solution ^{1}H spectrum of lysozyme is shown in black in all panels.

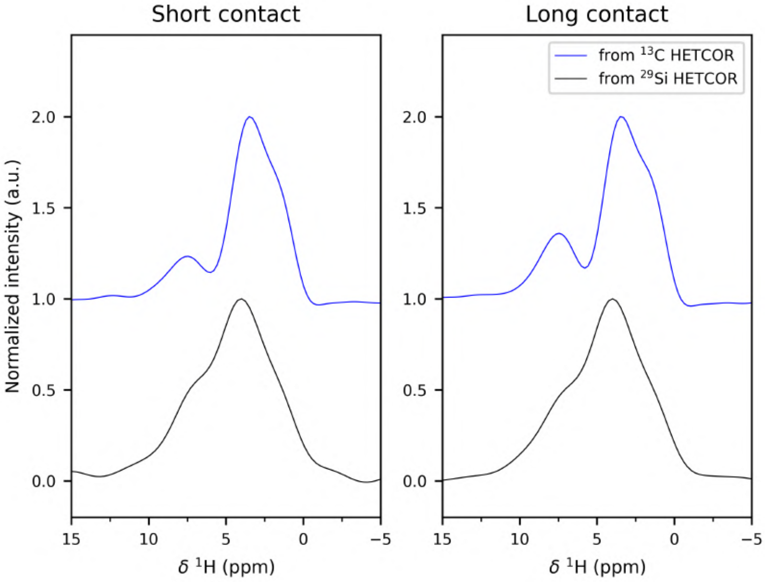

Figure 3.20: Comparison of the ^{1}H projections extracted from $\{^{1}H\}$-^{13}C HETCOR (blue) and $\{^{1}H\}$-^{29}Si HETCOR (black) spectra of the dry sample, at short (left panel) and long contact (right panel).

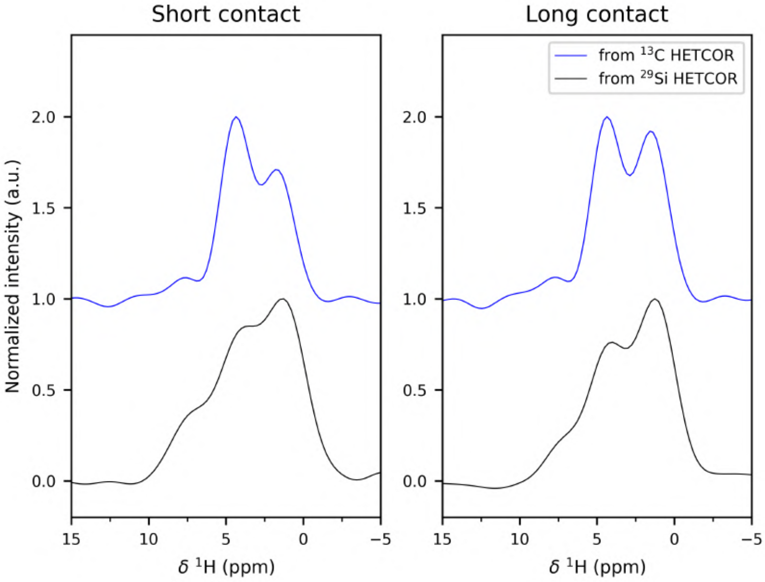

Figure 3.21: Comparison of the ^{1}H projections extracted from $\{^{1}H\}$-^{13}C HETCOR (blue) and $\{^{1}H\}$-^{29}Si HETCOR (black) spectra of the rehydrated withD$_2$O sample, at short (left panel) and long contact (right panel).

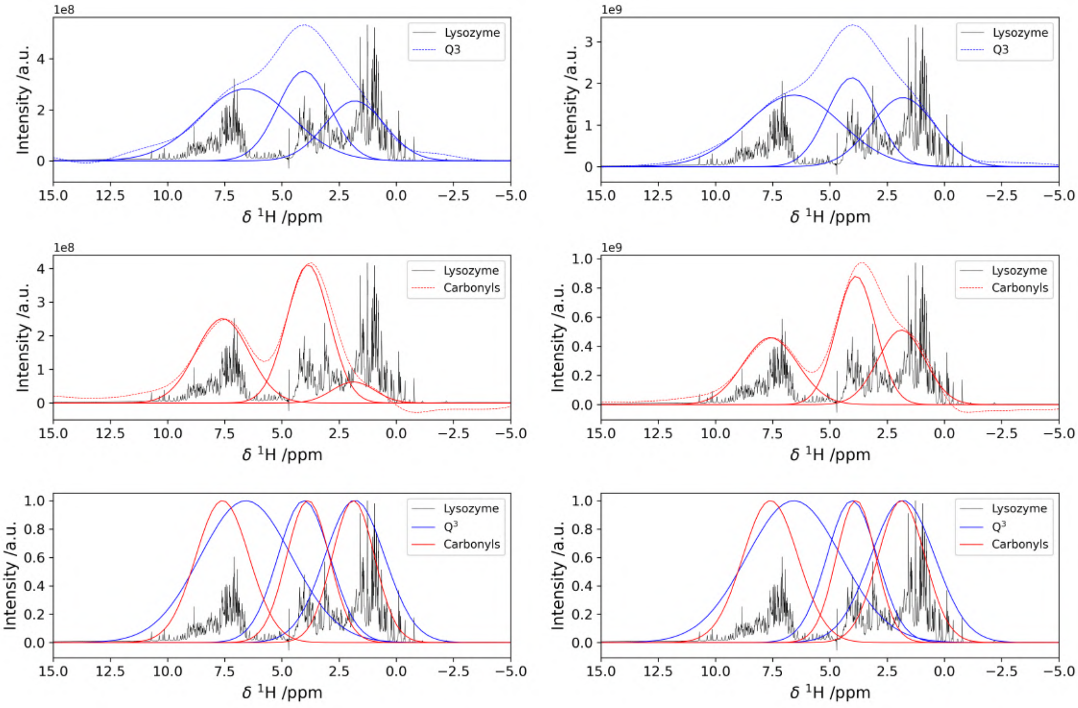

(a) **(b)**

Figure 3.22: (top) ^{1}H trace of the {^{1}H}-^{29}Si HETCOR acquired with 500 µs (**a**)/10 ms (**b**) of cross-polarization contact time on the freeze-dried sample. The signal is deconvoluted as a sum of three gaussian peaks. (middle) ^{1}H trace of the {^{1}H}-^{13}C HETCOR acquired with 150 µs (**a**)/1.5 ms (**b**) of cross-polarization contact time on the freeze-dried sample. The signal is deconvoluted as a sum of three gaussian peaks. (bottom) The two sets of gaussians fitting the {^{1}H}-^{29}Si and the {^{1}H}-^{13}C HETCOR traces, all reported to the same height. The parameters of the deconvolutions are shown in table 3.6.

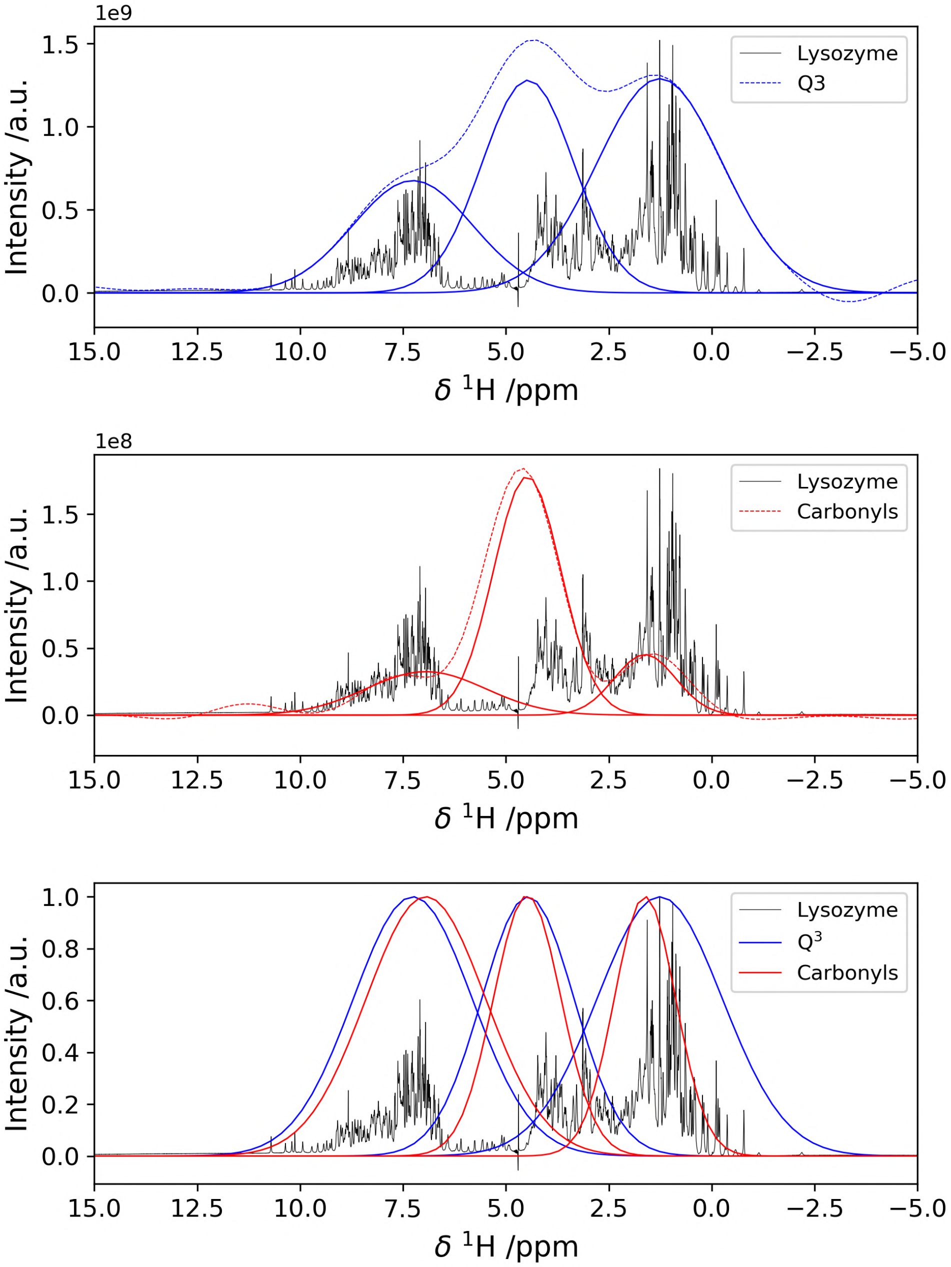

Figure 3.23: (top) ^{1}H trace of the $\{^1H\}$-^{29}Si HETCOR acquired with 500 µs of cross-polarization contact time on the rehydrated with D_2O sample. The signal is deconvoluted as a sum of three gaussian peaks. (middle) ^{1}H trace of the $\{^1H\}$-^{13}C HETCOR acquired with 150 µs of cross-polarization contact time on the rehydrated with D_2O sample. The signal is deconvoluted as a sum of three gaussian peaks. (bottom) The two sets of gaussians fitting the $\{^1H\}$-^{29}Si and the $\{^1H\}$-^{13}C HETCOR traces, all reported to the same height. The parameters of the deconvolutions are shown in table 3.7.

3.6 Doping with metals

In order to provide a metal functionalization, the lys-SiO_2 composite has been prepared as explained in section 2.1.1. All the ssNMR spectra acquired on those samples, freeze-dried, revealed the same appearance and relative intensities of the lys-SiO_2 dry composite prepared in aqueous solutions, but with a dramatic decrease of signal to noise ratio. This effect, induced by the increase of relaxation rates due to the presence of a paramagnetic centre in the sample (*paramagnetic relaxation enhancement*), is a hint of segregation of metals and silica in the sample, rather than a true integration inside the composite structure[71,72].

However, this behaviour should be better understood, and further experiments are needed.

3.7 Electrochemical measurements

The cyclic voltammetry of TiO_2 on the ITO electrode, reported in figure 3.24, was made to verify the absence of disruptors or electroactive species on the electrode surface. The voltammogram has been smoothed with a Savitsky-Golay filter. It shows a small peak around 0.2 V in the forward scan, that may be ascribable to lysozyme residuals, or could be just a noise artifact, given the extremely low detected currents. Overall, the CV appears quite clean.

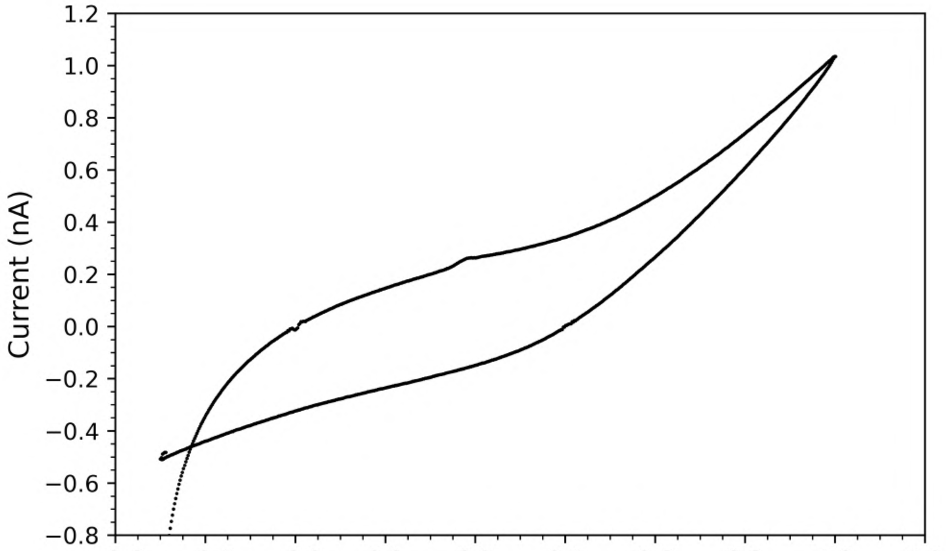

Figure 3.24: Cyclic voltammetry of titania deposited on the ITO electrode. The potential has been varied from $-0.5\,\mathrm{V}$ to $1\,\mathrm{V}$ with a scanning rate of $50\,\mathrm{mV\,s^{-1}}$.

The chronoamperometric measurement at 0 V is shown in figure 3.25. After the time required for the current to stabilize (about three minutes), the sample shows an increase of the current when the electrode is irradiated with UV light, whereas it returns to the original values when the light is turned off. The average current gap is 35.7(1) nA.

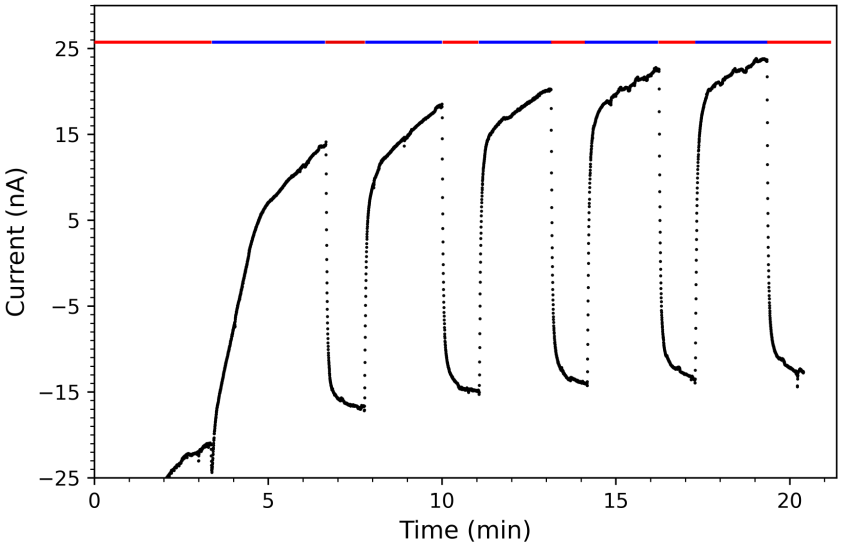

Figure 3.25: CA at 0 V of the ITO electrode coated with TiO_2. The coloured line at the top shows the status of the UV lamp: red − off, blue − on.

Being these peaks anodic, and therefore associated to oxidation phenomena, they are accentuated at positive potential.

In order to confirm this feature, two more chronoamperometries have been performed at 0.3 V and −0.3 V. The data are shown in figure 3.26a and 3.26b, respectively. As expected, when a positive potential is applied to the sample, the increase of current is greater than in the 0 V case, whereas when a negative potential is applied the current gap is smaller.

A summary plot is reported in figure 3.27.

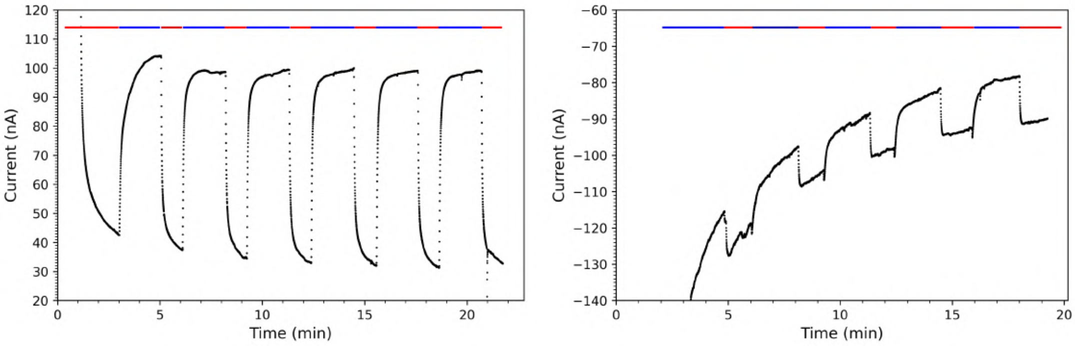

(a) Current gap: 64.6(28) nA

(b) Current gap: 17.0(10) nA

Figure 3.26: CA at 0.3 V (**a**) and at −0.3 V (**b**) of the ITO electrode coated with TiO_2. The coloured line at the top shows the status of the UV lamp: red − off, blue − on.

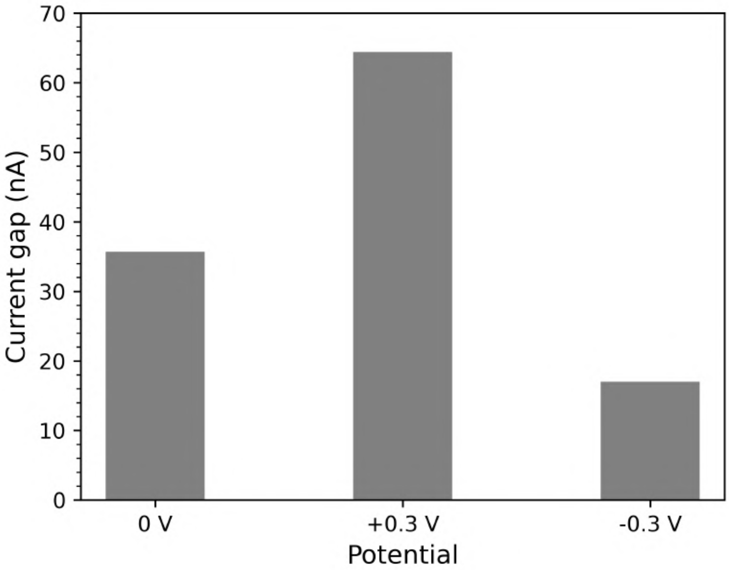

Figure 3.27: Comparison plot of the current gaps observed in the chronoamperometric measurements at different potentials.

4. Conclusions

In this thesis work the synthesis of a lysozyme-silica composite has been successfully achieved through a sol-gel process. By mixing silica precursors with silica in a buffer solution, the generation of silica particles of about 50 nm in diameter is observed in few seconds. The same procedure has been employed for the synthesis of a lysozyme-titania composite, that ended up with the generation of much smaller TiO_2 nanoparticles, about 10 nm in diameter.

According to the performed experiments, in the first composite lysozyme is found for the 20% bound to the silica surface by electrostatic interactions, while the remaining 80% is trapped inside the inorganic matrix and cannot exit without full denaturation of the protein. Interestingly, the same experiments produced different outcomes in the lysozyme-titania composite, therefore the relative arrangement of protein and TiO_2 remained ambiguous. Further analysis will be carried out in future in order to sort this out.

Silica particles form a quite condensed network, similar to PL-12 silica and SBA-15 silica, and lysozyme maintain its folding even when inside the composite.

Through the ssNMR analysis of the composite it resulted that there are not covalent interactions between the protein and the condensed inorganic material, but they remain in tight contact with each other through the surface sites of the matrix. The fact that lysozyme can only be quantitatively removed from silica by denaturation, regardless of the ionic strength of the medium, suggests that the protein is actually trapped inside the silica by mostly steric effects.

The attempts to functionalize the composite with vanadium, cobalt and copper have had no effect, since the metal cations were not integrated in the structure.

The cyclic voltammetry performed on the ITO/TiO_2 sample seemed to confirm the presence of a semiconductive titania layer. The enhancement in current flowing under UV light radiation has been observed in the chronoamperometric analysis, which show a current gap of around 36 nA when a 0 V potential is applied. Besides this result clearly demonstrate the feasibility of the photocatalytic device project, the current gap are still too small. The main reason may be the little amount of material that was actually deposited on the substrate, therefore further advancement in this sense can be done optimizing the deposition protocol by working on concentration and volume of the solutions.

In conclusion, we demonstrated the capability of ssNMR to investigate the nature of the interactions that exist between the components of this kind of composite materials. Following the guidelines given by this work, a future perspective will be the development of a composite material based on cytochrome-c and titania, in order to create a photoactive catalyst for oxidation reactions of organic pollutants. We will have to deal with the complications that the presence of iron and the analysis of $^{47/49}$Ti ssNMR spectra will matter, but the results reported herein constitute a very good starting point for this project.

A. Solid State Nuclear Magnetic Resonance

Nuclear Magnetic Resonance is a spectroscopic technique which observes nuclear spin transition in the nuclear ground state in presence of a static magnetic field. It gives information on the nature and on the chemical behaviour of the environment of single atoms, by looking how the electronic structure changes the energy of each nuclear spin transition.

Nuclear interactions are, in general, anisotropic, i.e. they depend on the orientation of the molecule with respect to the magnetic field. In a powder sample these interaction are not mediated by fast molecular motions, as it happens in solution, and therefore the resulting NMR spectra are very complicated.

In order to sort this out, the solid sample is packed in a rotor and spinned at very high frequency (magic angle spinning, MAS). In this way it is possible to remove artificially most of the aforementioned effects, making the solid state spectrum look like a solution one (table A.1).

The MAS frequency should be of the order of the interaction frequency that one wants to eliminate. This necessarily limits the amount of available sample, therefore reducing the sensitivity of the experiment (table A.2, figure A.1). Furthermore, the recoupling efficiency depends on the MAS frequency by a factor $\omega_{\mathrm{MAS}}^{-2}$, hence fast spinning might cause loss of information.

Interaction	Orientation dependence	Mediated to
Chemical shielding	$3\cos^2\theta - 1$	Chemical shift
Dipolar shielding	$3\cos^2\theta - 1$	Pseudocontact shift
Heteronuclear dipole-dipole	$3\cos^2\theta - 1$ 0	
Nuclear quadrupole (1st order)	$3\cos^2\theta - 1$ 0	
Nuclear quadrupole (2nd order)	$35\cos^4\theta - 30\cos^2\theta + 3$ Not averaged by MAS, but scaled to -7/18 of the static value. The isotropic value is named quadrupolar shift	
Contact shielding	$3\cos^2\theta - 1$, anisotropic only when caused by spin-polarization	Contact shift

Table A.1: Spatial dependence of nuclear interaction and their rotational average. Adapted from[73].

Outer diameter (mm)	Inner radius (mm)	Inner volume (mm^3)	Max. spinning rate (kHz)
4.0	1.50	52	15
3.2	1.06	22	23
1.3	0.35	2	60

Table A.2: Characteristics of some of the commercially available rotors for MAS NMR.

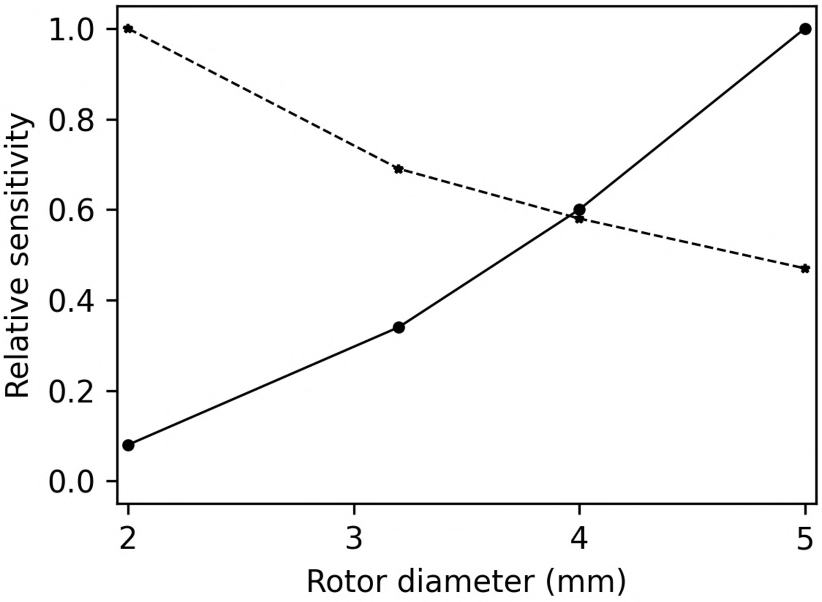

Figure A.1: Comparison of the probe sensitivity for different dimensions of employed rotor: relative sensitivity of the entire rotor (solid line) and relative sensitivity for unit volume (dashed line)[74].

A.1 Cross-polarization

Cross-polarization is a base element of solid state NMR experiments of insensitive nuclei, that is based on the magnetization transfer from more sensitive nuclei present in higher concentration, in order to increase the acquired signal[75,76]. The magnetization transfer happens through dipolar coupling between the less sensitive nuclei (I) and the more sensitive nuclei (S). A further requirement to perform this experiment is that the homonuclear coupling $I-I$ has to be negligible with respect to the $S-S$ coupling (i.e. the insensitive nuclei have to be diluted in the sample).

The system can be described in terms of spin thermodynamics, in which the S and I nuclei represent two thermal reservoirs at different temperatures. Both of them are in contact with the environment, that is at room temperature. Establishing a thermal contact between the two reservoirs, energy transfer from the hot one (I) to the cold one (S) is obtained, resulting in a decrease of S spin temperature. In terms of spin energy levels, decreasing the temperature means to increase the population difference between the ground state and the excited state, therefore an increase of the intensity of the signal associated to the transition is observed.

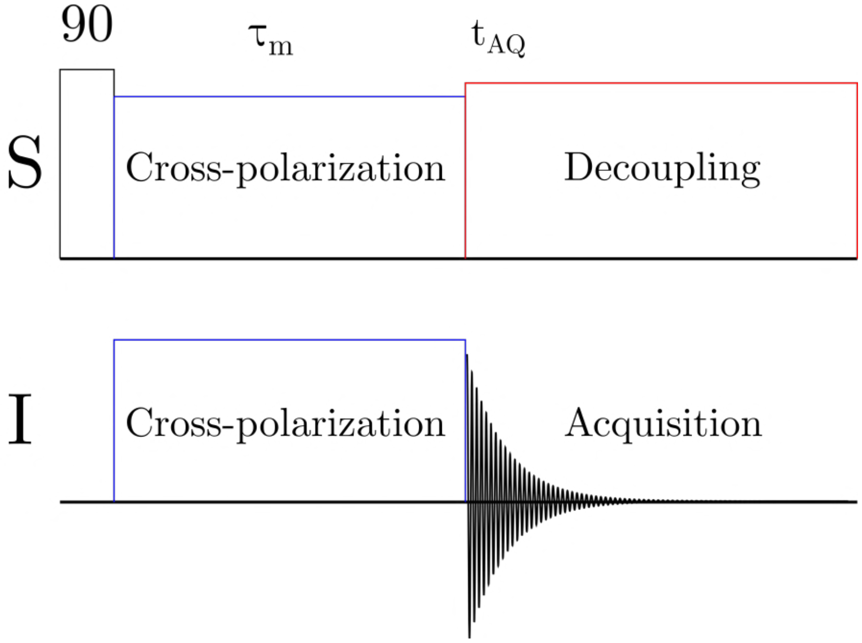

Figure A.2: Pulse program of a standard cross-polarization solid state NMR experiment.

When the system is at equilibrium, the splitting between the spin levels is determined by the intensity of the static magnetic field B_0: being the two nuclei different, the energy difference between the S and I state will be also different. During the mixing time τ_m of the experiment, a magnetic field B_1 is applied as spin-lock to both nuclei, so that they don't feel anymore the effect of B_0. Modulating the intensity of the spin-lock, it is possible to make the energy difference between the levels of each nucleus equal (Hartmann-Hahn condition): in these conditions, the magnetization transfer does not require any energy cost.

The increase of the I signal intensity is proportional to the γ_S/γ_I ratio: for this reason the maximum gain in intensity is achieved when the S nucleus is ^{1}H.

Furthermore, a decrease of the recycle delays of magnetization is observed, since the transversal relaxation time T_1 is driven by S relaxation.

The pulse program of the experiment is shown in figure A.2.

The optimal contact time τ_m depends on the speed of magnetization transfer, which is proportional to the strength of the heteronuclear coupling, and on relaxation time $T_{1\rho}$, that is accelerated by molecular motions in Larmor frequency timescales.

A homonuclear decoupling sequence has to be applied on the S spin in order to increase the resolution during the acquisition time.

Given the high power applied during this latter phase, the acquisition times must be as short as possible to avoid probe usure and sample heating. The recycle delays between two subsequent acquisitions are typically of the order of 3 s, however they are limited by transverse relaxation.

A.2 CPMG

When the sample has a long enough longitudinal relaxation time (T_2), it is possible to incredibly increase the number of scans, keeping the acquisition time reasonable, exploiting the Carr-Purcell-Maiboom-Gill (CPMG) experiment[77]. Through this pulse sequence, shown in figure A.3, the spectra are recorded in form of echo train, that consist in a first 90° pulse, followed by a series of 180° pulses that will generate an echo of the magnetization for each pulse. The echoes acquired in this way can be decomposed in "normal" FIDs and processed as classic NMR spectra.

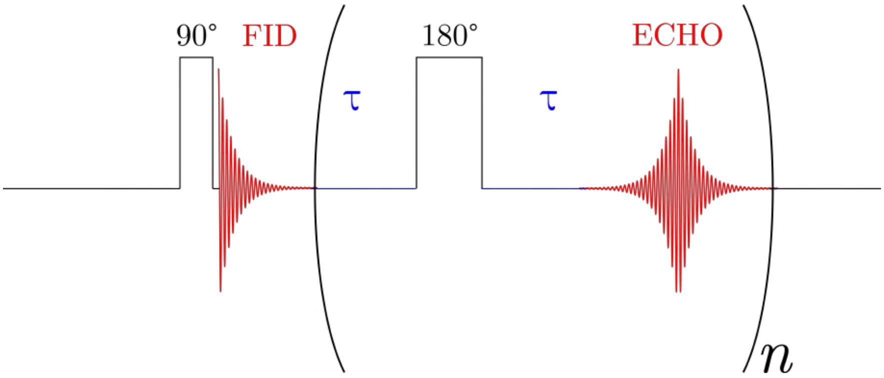

Figure A.3: Pulse program of a CPMG experiment.

The echo intensity depends on the magnetization present on the xy plane at the time of the acquisition, that is influenced by longitudinal relaxation. For this reason, only the first decay can be used for quantitative analysis, because the signals that compose the NMR spectra may relax at a different pace one from each other, and therefore varying the relative intensities of later echoes. However, the information on chemical shift, linewidths and lineshapes are conserved, making this a clever way to stabilize a fitting procedure.

Another processing option for the CPMG experiment consists in summing up the echoes in the time domain as they were scans of a NMR spectrum. In this way, it is possible to dramatically increase the intensity and the resolution of the NMR signal through a remarkable smoothing of the background noise.

A.3 PMLG

In order to increase the resolution of the signal, it is necessary to apply a homonuclear decoupling sequence at the more sensitive nucleus while the FID is recorded. In this work, the more evolute version of the simple Lee-Goldburg (LG) experiment, i.e. the Phase-Modulated Lee-Goldburg (PMLG) has been used[78].

The LG experiment is based on sending an off-resonance pulse, continuous, of frequency $\omega_1/\sqrt{2}$, where ω_1 is the spectrometer carrier frequency. In this way, the nuclear magnetization precesses in a reference frame disaligned with the laboratory frame, causing the average of the dipolar coupling at the first order to be null.

The subsequent evolution of LG is the Frequency Switch Lee-Goldburg (FSLG), where the frequency of the off-resonance pulse is alternated between $\pm\omega_1/\sqrt{2}$. With each frequency switch, a π phase shift is also introduced. To cancel the effect of the dipolar coupling, the inversions must be separated by the time that the nuclear magnetization takes to make a 2π precession in the tilted frame.

Since the FSLG consists of a very simple sequence, it has been modified to increase its performance, arriving to the development of the PMLG experiment. The PMLG sequence consists of a series of m pulses, each one with a different phase, that can be repeated n times. The phase increment is inversely proportional to the number of sent pulses. To keep the radiofrequency profile as regular as possible, a high number of pulses must be sent, reducing their duration, that has to be consequently regulated on the base of the spectrometer electronics to avoid the formation of artifacts.

This method is more versatile than FSLG, because it consents to modulate intensity and shape of the RF pulses.

A.4 Multivariate Curve Resolution

Multivariate Curve Resolution (MCR) is a chemometric method employed mainly for extracting information on the pure components from data acquired on complex mixtures through e.g. UV-visible spectroscopy and chromatography. In this thesis work, it has been employed as a denoising procedure for increasing the resolution of 2D solid state NMR spectra, applying the entire algorithm to the data in the time domain (i.e. FIDs), allowing the employment of further processings[39].

MCR decomposes the data matrix $\mathbb{D}$ (of dimensions $m \times n$) in a "concentration" matrix $\mathbb{C}$ (of dimensions $m \times k$) and a matrix "spectra" $\mathbb{S}$ (of dimensions $k \times n$), leaving a residual matrix $\mathbb{E}$ (of dimensions $m \times n$).

$$\mathbb{D} = \mathbb{C}\mathbb{S}^T + \mathbb{E} \tag{A.1}$$

Intuitively, in a 2D NMR spectra there is not a concentration variation, but a variation in the intensity of the signals due to the evolution in the indirect dimension. Therefore, the $\mathbb{C}$ matrix contains the traces of the indirect dimension, whereas $\mathbb{S}$ contains the FIDs of the direct dimensions.

In order to generate an initial guess of the two matrices $\mathbb{C}$ and $\mathbb{S}$, the algorithm selects the purest columns and rows of $\mathbb{D}$ (the ones with less noise) and fills with them $\mathbb{C}$ and $\mathbb{S}$, respectively. The evaluation is done by means of a correlation matrix, and the determinants of its minors are used as weights. This step requires as input the number of pure components to look for (in this case, $k = 4$) and the maximum percentage of allowed noise (10%).

Obtained the initial matrices $\mathbb{C}_0$ and $\mathbb{S}_0$, MCR foresees an optimization phase, whose purpose is to fill the matrix $\mathbb{E}$, that at this point of the procedure is null. The optimization is made through an iterative cycle that, at the k-th step, consists of the steps shown in equation A.2.

$$\begin{aligned} \mathbb{S}_k^T &= \mathbb{C}_{k-1}^+ \, \mathbb{D} \\ \mathbb{C}_k &= \mathbb{D} \, \mathbb{S}_k^{T+} \\ \mathbb{E}_k &= \mathbb{D} - \mathbb{C}_k \, \mathbb{S}_k^T \end{aligned} \tag{A.2}$$

where the symbol "$^+$" denotes the Moore-Penrose pseudoinverse matrix.

The stopping criterion has been established on the base of the spectral norm of the difference of each of the three matrices between two subsequent iterations of the optimization:

$$\|\mathbb{C}_k - \mathbb{C}_{k-1}\|_2 \leq 10^{-5} \quad \|\mathbb{S}_k - \mathbb{S}_{k-1}\|_2 \leq 10^{-5} \quad \|\mathbb{E}_k - \mathbb{E}_{k-1}\|_2 \leq 10^{-5} \tag{A.3}$$

If the condition A.3 is satisfied, the convergence is said to be achieved.

A peculiar feature of MCR is the possibility to co-process different spectra employing a common set of FIDs. In order to do this, it is necessary to concatenate the various datasets, creating a unique matrix that contains all of them, as shown in figure A.4.

Figure A.4: Concatenation of three datasets, $\mathbb{D}_1$, $\mathbb{D}_2$ and $\mathbb{D}_3$. A matrix with the same number of rows of each dataset and number of columns equal to the sum of the number of columns of all datasets is obtained. The columns of the $\mathbb{C}$ matrix (red) contains information relative to a single dataset, whereas the rows of the $\mathbb{S}^T$ matrix (blue) necessarily contain information of all of them.

B. Scanning Electron Microscopy

Scanning Electron Microscopy (SEM) is a technique that produces images of the sample by scanning its surface with a focused beam of electrons, and detecting the various signals originated by the interaction between these electrons and the sample. The information that can be derived from SEM images include surface topography and composition of the sample.

In a typical SEM setup, an electron beam is emitted from an electron gun and is focused by a series of condenser lenses to a spot of diameter between 0.4 and 5 nm. Then the beam passes through pairs of scanning coils or deflector plates which deflect the beam in order to scan in a raster fashion over a rectangular area of the sample surface.

The interaction volume of the specimen is the volume that electrons can reach inside the sample surface without losing all their energy because of random scattering and absorption phenomena, and normally extends from less than 100 nm to 5 µm.

The magnification in a SEM can be controlled over a range of six orders of magnitude by reducing the size of the raster on the specimen.

The most common detectors for the generation of images collect secondary electrons ejected from conduction or valence band of the specimen atoms by inelastic scattering interaction with the primary electron beam. The brightness of the signal depends on the number of secondary electron that reach the detector.

References

[1] Werner EG Müller et al. "Silicateins—a novel paradigm in bioinorganic chemistry: enzymatic synthesis of inorganic polymeric silica". In: *Chemistry–A European Journal* 19.19 (2013), pp. 5790–5804.

[2] Lorena Betancor and Heather R Luckarift. "Bioinspired enzyme encapsulation for biocatalysis". In: *Trends in biotechnology* 26.10 (2008), pp. 566–572.

[3] W Marner. "II, Shaikh AS, Muller SJ, Keasling JD". In: *Biomacromolecules* 9 (2008), p. 1.

[4] René Ullrich and Martin Hofrichter. "Enzymatic hydroxylation of aromatic compounds". In: *Cellular and Molecular Life Sciences* 64.3 (2007), pp. 271–293.

[5] Jenny Schneider et al. "Understanding TiO_2 photocatalysis: mechanisms and materials". In: *Chemical reviews* 114.19 (2014), pp. 9919–9986.

[6] Samira Bagheri, Nurhidayatullaili Muhd Julkapli, and Sharifah Bee Abd Hamid. "Titanium dioxide as a catalyst support in heterogeneous catalysis". In: *The scientific world journal* 2014 (2014).

[7] Lei Jin et al. "Highly Crystalline Mesoporous Titania Loaded with Monodispersed Gold Nanoparticles: Controllable Metal-Support Interaction in Porous Materials". In: *ACS applied materials & interfaces* 12.8 (2020), pp. 9617–9627.

[8] David M Antonelli and Jackie Y Ying. "Synthesis of a stable hexagonally packed mesoporous niobium oxide molecular sieve through a novel ligand-assisted templating mechanism". In: *Angewandte Chemie International Edition in English* 35.4 (1996), pp. 426–430.

[9] Do Trong On. "A simple route for the synthesis of mesostructured lamellar and hexagonal phosphorus-free titania (TiO2)". In: *Langmuir* 15.25 (1999), pp. 8561–8564.

[10] YQ Wang, XH Tang, and LX Yin. "WP Huang, YR Hacohen, A. Gedanken". In: *Adv. Mater* 12 (2000), p. 1183.

[11] C Jeffrey Brinker et al. "Evaporation-induced self-assembly: nanostructures made easy". In: *Advanced materials* 11.7 (1999), pp. 579–585.

[12] Renyuan Zhang et al. "Mesoporous titania: from synthesis to application". In: *Nano Today* 7.4 (2012), pp. 344–366.

[13] Peidong Yang et al. "Block copolymer templating syntheses of mesoporous metal oxides with large ordering lengths and semicrystalline framework". In: *Chemistry of Materials* 11.10 (1999), pp. 2813–2826.

[14] Bozhi Tian et al. "Fast preparation of highly ordered nonsiliceous mesoporous materials via mixed inorganic precursors". In: *Chemical Communications* 17 (2002), pp. 1824–1825.

[15] Wenbo Yue et al. "Mesoporous monocrystalline TiO2 and its solid-state electrochemical properties". In: *Chemistry of Materials* 21.12 (2009), pp. 2540–2546.

[16] Zhenyu Zhang, Fan Zuo, and Pingyun Feng. "Hard template synthesis of crystalline mesoporous anatase TiO 2 for photocatalytic hydrogen evolution". In: *Journal of Materials Chemistry* 20.11 (2010), pp. 2206–2212.

[17] L Saadoun et al. "1, 2-Diolates of titanium as suitable precursors for the preparation of photoactive high surface titania". In: *Applied Catalysis B: Environmental* 21.4 (1999), pp. 269–277.

[18] Jiaguo Yu et al. "Effects of acidic and basic hydrolysis catalysts on the photocatalytic activity and microstructures of bimodal mesoporous titania". In: *Journal of Catalysis* 217.1 (2003), pp. 69–78.

[19] Gunar Kaune et al. "Hierarchically Structured Titania Films Prepared by Polymer/Colloidal Templating". In: *ACS Applied Materials & Interfaces* 1.12 (2009). PMID: 20356168, pp. 2862–2869. DOI: `10.1021/am900592u`. eprint: `https://doi.org/10.1021/am900592u`. URL: `https://doi.org/10.1021/am900592u`.

[20] Akira Fujishima, Xintong Zhang, and Donald A Tryk. "TiO2 photocatalysis and related surface phenomena". In: *Surface science reports* 63.12 (2008), pp. 515–582.

[21] Masahiro Miyauchi et al. "Photoinduced surface reactions on TiO2 and SrTiO3 films: photocatalytic oxidation and photoinduced hydrophilicity". In: *Chemistry of Materials* 12.1 (2000), pp. 3–5.

[22] Yuri Hendrix et al. "Titania-silica composites: a review on the photocatalytic activity and synthesis methods". In: *World Journal of Nano Science and Engineering* 5.04 (2015), p. 161.

[23] Rong Wang et al. "Light-induced amphiphilic surfaces". In: *nature* 388.6641 (1997), pp. 431–432.

[24] Bunsho Ohtani, Yoshimasa Ogawa, and Sei-ichi Nishimoto. "Photocatalytic activity of amorphous- anatase mixture of titanium (IV) oxide particles suspended in aqueous solutions". In: *The Journal of Physical Chemistry B* 101.19 (1997), pp. 3746–3752.

[25] Bryan EG Lucier and Yining Huang. "Reviewing 47/49Ti Solid-State NMR Spectroscopy: From Alloys and Simple Compounds to Catalysts and Porous Materials". In: *Annual Reports on NMR Spectroscopy* 88 (2016), pp. 1–78.

[26] Carole C Perry and Tracey Keeling-Tucker. "Biosilicification: the role of the organic matrix in structure control". In: *JBIC Journal of Biological Inorganic Chemistry* 5.5 (2000), pp. 537–550.

[27] Werner Stöber, Arthur Fink, and Ernst Bohn. “Controlled growth of monodisperse silica spheres in the micron size range”. In: *Journal of colloid and interface science* 26.1 (1968), pp. 62–69.

[28] Mark T Anderson et al. “Effect of methanol concentration on CTAB micellization and on the formation of surfactant-templated silica (STS)”. In: *Chemistry of materials* 10.6 (1998), pp. 1490–1500.

[29] Ricky Curley, Justin D Holmes, and Eoin J Flynn. “Can sustainable, monodisperse, spherical silica be produced from biomolecules? A review”. In: *Applied Nanoscience* (2021), pp. 1–28.

[30] Niels Timmer et al. “Toxicity mitigation and bioaccessibility of the cationic surfactant cetyltrimethylammonium bromide in a sorbent-modified biodegradation study”. In: *Chemosphere* 222 (2019), pp. 461–468.

[31] Siddharth V Patwardhan. “Biomimetic and bioinspired silica: recent developments and applications”. In: *Chemical Communications* 47.27 (2011), pp. 7567–7582.

[32] Pascal J Lopez et al. “Mimicking biogenic silica nanostructures formation”. In: *Current Nanoscience* 1.1 (2005), pp. 73–83.

[33] Nils Kröger. “Prescribing diatom morphology: toward genetic engineering of biological nanomaterials”. In: *Current opinion in chemical biology* 11.6 (2007), pp. 662–669.

[34] Manfred Sumper, Sonja Lorenz, and Eike Brunner. “Biomimetic control of size in the polyamine-directed formation of silica nanospheres”. In: *Angewandte Chemie* 115.42 (2003), pp. 5350–5353.

[35] Igor E Pamirsky and Kirill S Golokhvast. “Silaffins of diatoms: from applied biotechnology to biomedicine”. In: *Marine drugs* 11.9 (2013), pp. 3155–3167.

[36] Nils Kröger et al. “Species-specific polyamines from diatoms control silica morphology”. In: *Proceedings of the National Academy of Sciences* 97.26 (2000), pp. 14133–14138.

[37] Manfred S Weiss, Gottfried J Palm, and Rolf Hilgenfeld. “Crystallization, structure solution and refinement of hen egg-white lysozyme at pH 8.0 in the presence of MPD”. In: *Acta Crystallographica Section D: Biological Crystallography* 56.8 (2000), pp. 952–958.

[38] Heather R Luckarift et al. “Rapid, room-temperature synthesis of antibacterial bionanocomposites of lysozyme with amorphous silica or titania”. In: *Small* 2.5 (2006), pp. 640–643.

[39] Francesco Bruno et al. “Multivariate Curve Resolution for 2D Solid-State NMR spectra”. In: *Analytical chemistry* 92.6 (2020), pp. 4451–4458.

[40] Toru Shiomi et al. “Biomimetic Synthesis of Lysozyme- Silica Hybrid Hollow Particles Using Sonochemical Treatment: Influence of pH and Lysozyme Concentration on Morphology”. In: *Chemistry of Materials* 19.18 (2007), pp. 4486–4493.

[41] Daniela B van den Heuvel et al. “Formation of silica-lysozyme composites Through co-Precipitation and adsorption”. In: *Frontiers in Materials* 5 (2018), p. 19.

[42] Tomasz M Stawski et al. “Mechanism of silica–lysozyme composite formation unravelled by in situ fast SAXS”. In: *Beilstein journal of nanotechnology* 10.1 (2019), pp. 182–197.

[43] PL Poole and JL Finney. “Hydration-induced conformational and flexibility changes in lysozyme at low water content”. In: *International Journal of Biological Macromolecules* 5.5 (1983), pp. 308–310.

[44] Tai Huang Huang et al. “High-resolution nitrogen-15 nuclear magnetic resonance studies of. alpha.-lytic protease in solid state. Direct comparison of enzyme structure in solution and solid states”. In: *Biochemistry* 23.25 (1984), pp. 5933–5937.

[45] Gerard S Harbison et al. “Solid-state carbon-13 NMR detection of a perturbed 6-s-trans chromophore in bacteriorhodopsin”. In: *Biochemistry* 24.24 (1985), pp. 6955–6962.

[46] Scott D Kennedy and Robert G Bryant. “Structural effects of hydration: Studies of lysozyme by 13C solids NMR”. In: *Biopolymers: Original Research on Biomolecules* 29.14 (1990), pp. 1801–1806.

[47] Roger B Gregory et al. “The influence of hydration on the conformation of lysozyme studied by solid-state 13C-nmr spectroscopy”. In: *Biopolymers: Original Research on Biomolecules* 33.4 (1993), pp. 513–519.

[48] Michele Auger et al. “Solid-state carbon-13 NMR study of a transglutaminase-inhibitor adduct”. In: *Biochemistry* 32.15 (1993), pp. 3930–3934.

[49] David L Jakeman et al. “Effects of sample preparation conditions on biomolecular solid-state NMR lineshapes”. In: *Journal of biomolecular NMR* 12.3 (1998), pp. 417–421.

[50] Jutta Pauli et al. *Sample optimization and identification of signal patterns of amino acid side chains in 2D RFDR spectra of the α-spectrin SH3 domain.* 2000.

[51] Rachel W Martin and Kurt W Zilm. “Preparation of protein nanocrystals and their characterization by solid state NMR”. In: *Journal of Magnetic Resonance* 165.1 (2003), pp. 162–174.

[52] Karsten Seidel et al. “High-resolution solid-state NMR studies on uniformly [13C, 15N]-labeled ubiquitin”. In: *Chembiochem* 6.9 (2005), pp. 1638–1647.

[53] Alexey Krushelnitsky et al. “Comparison of the internal dynamics of globular proteins in the microcrystalline and rehydrated lyophilized states”. In: *Biochimica et Biophysica Acta (BBA)-Proteins and Proteomics* 1764.10 (2006), pp. 1639–1645.

[54] Marco Fragai et al. “Practical considerations over spectral quality in solid state NMR spectroscopy of soluble proteins”. In: *Journal of biomolecular NMR* 57.2 (2013), pp. 155–166.

[55] Enrico Ravera. “The bigger they are, the harder they fall: A topical review on sedimented solutes for solid-state NMR”. In: *Concepts in Magnetic Resonance Part A* 43.6 (2014), pp. 209–227.

[56] Dabeiba Marulanda et al. "Magic Angle Spinning Solid-State NMR Spectroscopy for Structural Studies of Protein Interfaces. Resonance Assignments of Differentially Enriched Escherichia c oli Thioredoxin Reassembled by Fragment Complementation". In: *Journal of the American Chemical Society* 126.50 (2004), pp. 16608–16620.

[57] Enrico Ravera et al. "Biosilica-entrapped enzymes can be studied by DNP-enhanced high-field NMR". In: *Chemphyschem: a European journal of chemical physics and physical chemistry* 16.13 (2015), p. 2751.

[58] Nurit Adiram-Filiba et al. "Ubiquitin immobilized on mesoporous MCM41 silica surfaces–Analysis by solid-state NMR with biophysical and surface characterization". In: *Biointerphases* 12.2 (2017), p. 02D414.

[59] Jorge J Moré and Danny C Sorensen. "Computing a trust region step". In: *SIAM Journal on scientific and statistical computing* 4.3 (1983), pp. 553–572.

[60] Donald W Marquardt. "An algorithm for least-squares estimation of nonlinear parameters". In: *Journal of the society for Industrial and Applied Mathematics* 11.2 (1963), pp. 431–441.

[61] M Newville et al. *LMFIT: Non-Linear Least-Square Minimization and Curve-Fitting for Python, doi: 10.5281/zenodo. 11813*. 2014.

[62] Wolfgang Lutz et al. *Characterization of silica gels by 29Si MAS NMR and IR spectroscopic measurements*. 2009.

[63] Tommaso Martelli et al. "Atomic-Level Quality Assessment of Enzymes Encapsulated in Bioinspired Silica". In: *Chemistry–A European Journal* 22.1 (2016), pp. 425–432.

[64] Sean C Christiansen et al. "Sensitivity considerations in polarization transfer and filtering using dipole–dipole couplings: Implications for biomineral systems". In: *Solid State Nuclear Magnetic Resonance* 29.1-3 (2006), pp. 170–182.

[65] Dorothea Wisser et al. "1H–13C–29Si triple resonance and REDOR solid-state NMR—A tool to study interactions between biosilica and organic molecules in diatom cell walls". In: *Solid state nuclear magnetic resonance* 66 (2015), pp. 33–39.

[66] VM Mastikhin, IL Mudrakovsky, and AV Nosov. "1H NMR magic angle spinning (MAS) studies of heterogeneous catalysis". In: *Progress in nuclear magnetic resonance spectroscopy* 23.3 (1991), pp. 259–299.

[67] Hyun Na Kim and Sung Keun Lee. "Atomic structure and dehydration mechanism of amorphous silica: Insights from 29Si and 1H solid-state MAS NMR study of SiO2 nanoparticles". In: *Geochimica et Cosmochimica Acta* 120 (2013), pp. 39–64.

[68] Alexander J Vega and George W Scherer. "Study of structural evolution of silica gel using 1H and 29Si NMR". In: *Journal of Non-Crystalline Solids* 111.2-3 (1989), pp. 153–166.

[69] Chuanyu Yan, François Kayser, and Reiner Dieden. “Sensitivity enhancement via multiple contacts in the {1 H–29 Si}–1 H cross polarization experiment: a case study of modified silica nanoparticle surfaces”. In: *RSC Advances* 10.39 (2020), pp. 23016–23023.

[70] George D Cody, Bjorn O Mysen, and Sung Keun Lee. “Structure vs. composition: A solid-state 1H and 29Si NMR study of quenched glasses along the Na2O-SiO2-H2O join”. In: *Geochimica et Cosmochimica Acta* 69.9 (2005), pp. 2373–2384.

[71] Yamini S Avadhut et al. “Structural investigation of aluminium doped ZnO nanoparticles by solid-state NMR spectroscopy”. In: *Physical Chemistry Chemical Physics* 14.33 (2012), pp. 11610–11625.

[72] Wenyu Li et al. “Doping homogeneity in co-doped materials investigated at different length scales”. In: *Physical Chemistry Chemical Physics* 22.2 (2020), pp. 818–825.

[73] Ivano Bertini et al. *NMR of paramagnetic molecules: applications to metallobiomolecules and models*. Elsevier, 2016.

[74] Seth A McNeill et al. “Optimizing ssNMR experiments for dilute proteins in heterogeneous mixtures at high magnetic fields”. In: *Magnetic Resonance in Chemistry* 45.S1 (2007), S209–S220.

[75] David Marks and Shimon Vega. “A theory for cross-polarization NMR of nonspinning and spinning samples”. In: *Journal of Magnetic Resonance, Series A* 118.2 (1996), pp. 157–172.

[76] A Pines, M Go Gibby, and JS Waugh. “Proton-enhanced NMR of dilute spins in solids”. In: *The Journal of chemical physics* 59.2 (1973), pp. 569–590.

[77] JW Wiench, VS-Y Lin, and M Pruski. “^{29}Si NMR in solid state with CPMG acquisition under MAS”. In: *Journal of Magnetic Resonance* 193.2 (2008), pp. 233–242.

[78] Elena Vinogradov, PK Madhu, and Shimon Vega. “High-resolution proton solid-state NMR spectroscopy by phase-modulated Lee–Goldburg experiment”. In: *Chemical Physics Letters* 314.5-6 (1999), pp. 443–450.